Mari Skauge Størksen
Selma Aurora Lund

Hydraulic design of a turbine for energy recovery purposes

Masteroppgave

NTNU
Kunnskap for en bedre verden

Mari Skauge Størksen
Selma Aurora Lund

Hydraulic design of a turbine for energy recovery purposes

NTNU
Kunnskap for en bedre verden

Waterpower Laboratory

NTNU

Abstract

This master's will in collaboration with Framo AS focus on the hydraulic design of a complete Francis turbine for energy recovery purposes in offshore applications. The turbine design deviates from conventional models by its absence of a spiral casing and the fact that the stay vanes direct the flow from the gravitational direction and radially into the guide vanes. Adjustable guide vanes are implemented to accommodate a decline in flow rate. A numerical model is developed, considering high head Francis theory, constraints from Framo, and using computational fluid dynamics (CFD) analysis. The efficiency of the turbine is evaluated at different flow rates, demonstrating a close match to Framo's existing Sea Water Lift pump-turbine. Recommendations for improvement include enhancing the stay vanes' performance by making longer vanes and curving them further upstream, optimizing the design of guide vanes to minimize separation of flow, and investigating the runner's pressure distribution to mitigate potential issues like vibrations and resonance. The findings contribute to understanding turbine performance and provide valuable insights for future optimization and design refinements.

Vannkraftlaboratoriet

NTNU
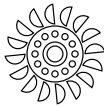
Sammendrag

Denne masteroppgaven fokuserer på design og analyse av en komplett Francis-turbin for Framo AS med formål om energiutvinning i offshore-applikasjoner. Turbindesignet skiller seg fra konvensjonelt design ved at den ikke har spiraltromme, samt at stagskovlene leder vannet fra gravitasjonsretningen og radielt inn i ledeskovlene. Justerbare ledeskovler er inkludert for å tilpasse seg et kjølebehov med minkende vannstrøm. En numerisk modell er utviklet, basert på høytrykks Francis-teori og begrensninger fra Framo. Virkningsgraden til turbinen er evaluert ved ulike strømningshastigheter, og er nærliggende virkningsgraden til Framos eksisterende Sea Water Lift-pumpeturbin. Det er anbefalt å forbedre stagskovlenes ytelse ved å forlenge bladene og kurve dem lenger oppstrøms, optimalisere designet av ledeskovlene for å minimere strømningsseparasjon, og undersøke trykkfordelingen på løpehjulet for å begrense potensielle problemer som vibrasjoner og resonans. Funnene bidrar til forståelse av turbinens ytelse og gir verdifull innsikt for fremtidig optimalisering og designforbedringer.

Acknowledgments

Contents

x

List of tables

List of figures

Nomenclature

Abbreviation

BEP   Best efficiency point

CFD   Computational Fluid Dynamics

FPSO   Floating, production, storage and offloading

GCI   Grid convergence index

GVO   Guide vane opening

NPSH   Net positive suction head

NTNU   Norwegian University of Science and Technology

RANS   Reynolds-averaged Navier-Stokes equation

SST   Shear stress transport

SWL   Sea water lift

Latin symbols

A Area (m^2)

c Absolute velocity (m s^{-1})

D Diameter (m)

f Frequency (Hz)

g Gravity acceleration (m s^{-2})

H Head (m)

I Inertia (kg m^2)

k Turbulent kinetic energy (m^2 s^{-2})

L Length (m)

n Rotational speed (s^{-1})

P Power (W)

p Pressure (Pa)

Q Flow rate (m^3 s^{-1})

q load (mPa)

r Radius (m)

M Torque (Nm)

S Streamline (-)

t Thickness (m)

u Peripheral velocity (m s^{-1})

w Relative velocity (m s^{-1})

Z Number of blades/guide vanes

Greek symbols

α Guide vane angle (°)

β Blade angle (°)

δ Lean angle (°)

η Efficiency

ϵ Rate of dissipation of turbulent kinetic energy (m^2 s^{-3})

γ Draft tube angle (°)

ρ Density (m^2 s^{-1})

σ Bending stress

θ Runner angle (°)

Ω Speed number (-)

ω Angular speed (rad s^{-1}), Turbulent frequency (s^{-1})

Superscripts and subscripts

1,2,...   Indices

accel   Acceleration

atm   Atmospheric

c   Cone

gv   Guide vane

grid   Grid

h   Hydraulic

max   Maximum

min   Minimum

rb   Runner blade

r   Required

s   Submerged

sec   Section

*   Best efficiency point

va   Vapor

———————— Chapter 1————————

Introduction

1.1 Background

In 2015 several countries committed to acting jointly to keep the global temperature rise below two degrees by signing the Paris Agreement [4]. Consequentially, all industries are required to map their emissions and look for ways to save energy. As the oil and gas industry is responsible for a quarter of Norway's greenhouse emissions every year, it is crucial that they constantly address the energy-saving potential in their production lines [5]. Floating Production, Storage, and Offloading vessels (FPSOs) are often located too far from the coastline to connect to the power grid and are therefore powered by gas turbines. This alone stands for about 80% of emissions from offshore activities [6], which has great potential in energy savings. Thus companies, such as Aker BP, SBM Offshore, and Yinson, aim for their FPSO activity to be net-zero by 2050 [7–9].

As a contribution, Framo AS is investigating the possibility of installing submerged turbines for energy recovery purposes onboard FPSOs [3]. For various cooling water purposes, a continuous amount of seawater is pumped up to the deck. Once the water has served its purpose it is dumped back into the sea, leaving a substantial amount of energy unexploited. According to their own calculations, the installation will generate about 30% of the energy used for pumping, reducing CO2 emissions by 3000-5000 tons per year.

The state-of-the-art consists of an unconventional inlet and no spiral casing, guide vanes, or draft tube. As included in Figure A.1 it provides an efficiency η of 84.4% and is dimensioned to accommodate a flow rate of 2.5 m^3/s and a head of 60 mlc. However, the design does not account for the predicted decrease in flow rate as the FPSO age. A study of a complete design including adjustable guide vanes is therefore requested, and a meridional

view of the reference design used in this thesis is presented in Figure A.2.

1.2 Objective

The objective of this thesis is to establish a numerical model of a complete Francis turbine, considering a set of stay vanes, adjustable guide vanes, a runner, and a draft tube. The design is based on high-head Francis theory, design limitations, and computational fluid dynamics (CFD) analysis. An efficiency study is done for different flow rates.

1.3 Outline

The thesis is structured as follows.

- Literature review

- Theory and methodology describing CFD theory and Francis turbine design.

- Results and discussions structured in final geometry, verification of the computational model, and lastly CFD results.

- Conclusions

- Future work

- References

- Appendix

————————— Chapter 2—————————

Literature review

Tiwari et. al [10] performed a multi-fidelity CFD analysis of a complete Francis turbine assembly during different load operations. The high-fidelity analysis concerned a geometry developed in Ansys Design Modeler and the flow path in ANSYS TurboGrid and was verified with experimental data. The low-fidelity analysis was done by discretizing the domain and performing a cascade analysis. The hydraulic efficiency from the different analyses showed a fair agreement. It was however emphasized that the low-fidelity analysis is highly influenced by the initial guess. Hence, due to its efficiency in terms of time and cost, it is an important asset for optimization purposes, but it relies on high fidelity analysis.

With the intention of establishing an optimum operating regime for a low head Francis turbine prototype, Tiwari et. al [11] investigated the same case above further. A detailed head loss analysis showed that the runner and draft tube are the most critical components of the turbine. The study concluded that higher speed factors are more detrimental than lower, and that part load operations are the most sensitive to higher speed factors and thus incur maximum losses.

Ayli et. al [12] investigated the effects different design parameters have on the Francis turbine runner performance. The lean angle between the hub and shroud, δ, was found to be important regarding the pressure balance in the runner. It was concluded that if negative pressure regions that influence the generated power and efficiency occur, a lean from the hub in the direction of the rotation can increase the performance. However, a lean from the shroud in any direction is a sufficient solution to negative pressure gradients in the shroud layer.

The lean angle was also investigated by Ma et. al [13] for a low-head

Francis turbine runner. They discovered that if the lean from the shroud to the hub is negative to the runner rotation, the pressure load increase and decrease, respectively.

In 2020, Tiwari et. al [14] investigated the occurrence of cavitation in a low head Francis turbine prototype. To imitate a cavitating behavior and identify cavitation-prone areas, a homogeneous multiphase flow in terms of a continuous water phase and a dispersed vapor phase was selected. During part load, it was observed that runner core cavitation arose. This led to higher vapor volume fractions in the draft tube and it was clear that the inner bend was more susceptible to the phenomenon as it was exposed to a sudden change in flow direction.

To optimize the present design, the key findings from the studies mentioned above should be considered. As it is of interest to investigate the performance during part load, understanding and mitigating the impact of runner core cavitation should be a primary focus. Additionally, the lean angle between the hub and shroud should be carefully considered, as specific lean directions can significantly improve pressure balance and power generation.

—————————— Chapter 3——————————

Theory and methodology

This chapter will present CFD theory and Francis turbine design theory, and describing how this is applicable for the present thesis, taken into account the design limitations present.

3.1 CFD theory

CFD is a computational analysis tool for fluid flows, heat transfer, chemical reactions, etc. [15]. It involves finding numerical solutions to the Navier-Stokes equations of a specific volume of fluid. By identifying local characteristic variables, such as pressure, temperature, and velocity, it is possible to predict the behavior of complex flow patterns. Several CFD software has been developed, but for the purposes of this thesis, the following focus is on Ansys CFX and its associated theories.

Ansys CFX uses the finite volume method to solve partial differential equations (PDE), which involves dividing the computational domain into discrete control volumes [16]. All equations are solved iteratively. The method is considered well-established since it incorporates the principles of mass, momentum, and energy conservation within each control volume. The quality of the final results is governed by the element size. In principle: the smaller the element the more accurate the solution. However, this comes with a higher computational cost. Additional details regarding mesh generation are discussed in subsection 3.1.2.

Prior to the CFD simulation, it is essential to clearly define the problem by identifying the relevant physical phenomena involved. Furthermore, the success of a simulation relies on achieving mesh independence and establishing a correlation with experimental data. This, along with an explanation

of the simulation setup in Table 3.1, is presented in this section.

Table 3.1: Ansys CFX setting report

Parameter	Description
Analysis type	Steady-State
Interfaces	Frozen rotor, General connection: GGI
Material	Incompressible Newtonian fluid: Water
Boundary conditions	Inlet: Total pressure 588600 Pa, turbulence intensity 5%
	Outlet: Mass flow rate 2500 kgs^{-1}
	Reference pressure: 1 atm
	Walls: No slip, smooth
Discretization	Advection scheme: High resolution
	Turbulence numerics: First order
Turbulence models	$k - \omega$ SST with automatic wall function
Convergence control	RMS og pressure and momentum with target 1E-4
Timescale	0.01 s

As the thesis does not concern start-up and shut-down procedures, nor vortex investigations, a steady-state approach is employed. However, steady-state solvers are likely to diverge and need stabilization to achieve a solution [17]. Ansys CFX uses a pseudo-transient approach as an alternative to relaxation [16]. This involves adding an artificial time derivative to the PDE for each cell in the mesh. In principle, a modified steady-state equation is solved iteratively with an incremented pseudo-time step, which does not change the solution. However, time-dependent phenomenons, such as vortex shedding, are captured in the solution.

3.1.1 Turbulence modeling

In fluid mechanics, the motion of fluid is classified into two distinctly different regimes: One where the flow appears constant and smooth, and one where it follows irregular paths. The regimes are called laminar and turbulent, respectively. The hydrodynamic quantities, such as velocity, pressure, and temperature, of a turbulent flow fluctuates with time, which is usually handled through Reynolds decomposition. The method divides the quantity into a mean value and a fluctuating value. As CFX uses the pseudo-transient approach, time derivatives must be considered. [15, 18]

For an incompressible Newtonian fluid, such as water, four equations are

governing the mean flow: the continuity equation and the three Reynolds-averaged Navier-Stokes (RANS) equations. Regardless, there are ten unknowns: the pressure, three components of the velocity, and six components of the Reynolds stress. Since there are more unknowns than equations, the system is not closed. This is colloquially known as the closure problem of turbulence, which has given rise to turbulence modeling. [15]

Ansys CFX is able to simulate turbulence using different two-equation turbulence models, such as $k - \epsilon$, $k - \omega$, and the $k - \omega$ based shear stress transport (SST) model. The k in this context stands for turbulent kinetic energy. Two equation turbulence models consist of two additional transport equations allowing them to consider historical influences such as the convection and diffusion of turbulent energy. The purposed models are still an active area of research, as mentioned several times in chapter 2, and are therefore considered in the following theory. [15]

The $k - \epsilon$ model

The $k - \epsilon$ model solves the turbulent kinetic energy k, and the turbulent dissipation ϵ [19]. The original model was developed by Launder and Sharma (1974) but has been optimized several times since. In the industry, it is commonly used to predict mean properties in the free stream region. It tends to show poor performance when used on complex flows, such as when severe pressure gradients, separation, and/or unsteadiness interfere.

The $k - \omega$ model

Opposite to the $k - \epsilon$ model, Wilcox presented a two-equation model called the $k - \omega$ model as it solves for both k and the turbulent frequency ω [20]. The model captures the diversity of the turbulent flow and is able to describe the viscous boundary layers. It will also show if any adverse pressure gradients occur. Thus, the highly sensitive method requires a great amount of computational memory and simulation time.

The $k - \omega$ based SST model

In 1994, Menter proposed the $k - \omega$ based SST model as a contribution to the inadequate models above [15]. It retains the $k - \omega$ properties at the viscous sub-layer and gradually adapts $k - \epsilon$ properties as it approaches the free stream region. It requires an incompressible and single-phased flow. The Reynolds stress that occurs in the rotating system is captured by this model. The model is therefore found to be the most suitable model for this project.

7

3.1.2 Mesh generation

In CFD, a mesh is used to describe a discretized geometric domain. It involves dividing it into smaller, simpler quantities called elements, which again are connected by nodes. There are two types of approaches concerning discretizing: a structured and an unstructured mesh. A structured mesh is recognized by its uniform grid spacing and aligned elements, while an unstructured mesh is dominated by an irregular agreement of both nodes and elements. The reliability provided by the structured mesh allows the memory and simulation time to be the most efficient, while the unstructured mesh can generate geometries with higher complexity. The following theory will concern the settings available in Ansys TurboGrid [21] and Ansys Mesh [22], as they are used in the thesis.

To evaluate the quality of the mesh, Ansys uses a spectrum called mesh metrics. It concerns the element quality, the aspect ratio calculation for triangles, the aspect ratio calculation for quadrilaterals, the Jacobian ratio, the warping factor, the parallel deviation, the maximum corner angle, the skewness, and the orthogonal quality. In principle, simpler choices, such as the first element offset near wall element size and growth rate, must be evaluated. The first element offset near wall element size can either be absolute or refined with respect to y^+. The parameter represents a non-dimensional wall-to-grid distance [15]. Regardless of the decision, one must be aware of the consequences during grid refinement. An absolute element size will provide independent parameters close to the walls, while the refined element size will result in the turbulence model behaving differently. This thesis is based on an absolute value, and hence values like the blade loading cannot be used as a comparison. A growth rate of 1.2 is considered acceptable in most turbomachinery cases[1]. The parameter represents the increase in element size from the edge.

Mesh algorithms

Several combinations of the shape and distribution of elements are categorized as different algorithms. One of the most recognized is called the Sweep method. It generates a complete mesh by targeting one surface and duplicating it along the geometry, based on a number of mesh divisions chosen by the user. Thus, the cross-section is required to be identical. For "unsweepable" geometries, the Hex Dominant method is often recommended. It generates a mesh, as the name suggests, by mostly hexahedral elements. To handle cases in which the simulation time weighs more than the accuracy,

---

[1]Personal conversation with Trivedi [23]

it is possible to balance it with the Tetrahedrons method. For geometries that consist of both regions with and without identical cross-sections, the MultiZone method can be useful. By default, it provides a pure hexahedral mesh, and a manual selection of structured regions is possible.

As the name indicates, the Patch Conforming Method creates a mesh from the information of the faces and edges and then moves inwards the volume by conforming each boundary. The algorithm is known to generate a high-quality mesh. Opposite, we have the Patch Independent Method which targets the volume as a whole first and then projects to the details. Hence, geometrical features are not always accounted for, and the final mesh is consequently of poor quality.

3.1.3 Verification of computational domain

A converged solution does not necessarily imply a correct answer, it has to be verified and validated as well. Verification in this context is the process of checking that the simulation converges and is independent of the grid refinement while validating is whether the solution corresponds to physical measurements. However, no experimental data are available for this project, and thus validating the solution is not considered.

Grid independence study

Grid independence study is a crucial preliminary in all CFD cases to assure that the solution remains unaffected by grid refinement. General acceptance is that if domains are interconnected and significantly influence each other then a discretization study should be performed for all domains included[2]. Initially, a Grid Convergence Index (GCI) analysis was attempted for the unit, as it is considered a well-established approach in the industry [24]. However, Ansys TurboGrid was not able to generate the required refinement. Due to the great effort and time invested in the analysis, it is described in Appendix D. Thus, a simplified approach based on the finest available refinement in Ansys TurboGrid was conducted. It involved evaluating the convergence of a parameter Φ relevant to the case, for at least three different mesh sizes. As explained in subsection 3.1.2, it is not applicable to choose a Φ which is dependent on values close to the boundary as an absolute first element offset near wall element size is chosen. Other values, which are not directly affected by the near wall treatment, such as

---

[2]Personal conversation with Trivedi [23]

the cross-section pressure, are more suitable[3].

Residuals

A residual is defined as the local imbalance at each control volume of the modeled physical quantity [25]. In simpler terms, the smaller the residual the more steady the scheme. When the residuals converge, it indicates that the simulation has been iterated for a significant number of steps, thereby approaching a solution. The convergence usually involves reaching a certain order of magnitude, often of third or fourth order.

An alternative approach to determine iterative convergence is to study the convergence of a relative variable such as thrust, drag, or lift [26]. The convergence of the target is often related to the acceptable error in the variable used. This is a way to check whether the simulation has run for a sufficient number of iterations or not.

3.2 Francis turbine design

In turbomachinery, turbines are commonly divided into impulse and reaction-type turbines [27]. An impulse turbine functions by converting kinetic energy into mechanical energy through the rotation of a rotor. Reaction-type turbines convert both the kinetic energy and the pressure difference between the inlet and outlet to mechanical energy. In a Francis turbine, which is categorized as a reaction type, all blade channels in the runner are filled with water simultaneously. Hence, a complete flow analysis is necessary [28]. The key parameters head H and flow rate Q are used to find the available power in the water, given by Equation (3.1).

$$P = \rho g H Q \eta_h \tag{3.1}$$

η_h is the hydraulic efficiency accounting for friction losses in the runner, ρ is the density of the water and g is the gravitational acceleration. The power of a rotating shaft is given by $P = M\omega$, where M is the torque and ω is the angular velocity, given by the product of the radius and peripheral velocity. As it is of interest to investigate the turbine efficiency η, a relation between the shaft power and available power is introduced [2].

$$\eta = \frac{M\omega}{\rho g H Q \eta_h} \tag{3.2}$$

---

[3]Personal conversation with [23]

For reference, a typical Francis turbine has an efficiency between 80% and 95% [29]. It is important to note that a positive flow rate does not always indicate positive efficiency. As shown in Figure 3.1, the efficiency depends on the guide vane opening (GVO) while keeping the rotational speed n constant. A negative efficiency indicates that the flow rate is too low for the present blade design and the turbine creates a suction to get enough water through the runner. In such cases, the turbine operates in a reverse pump mode[4].
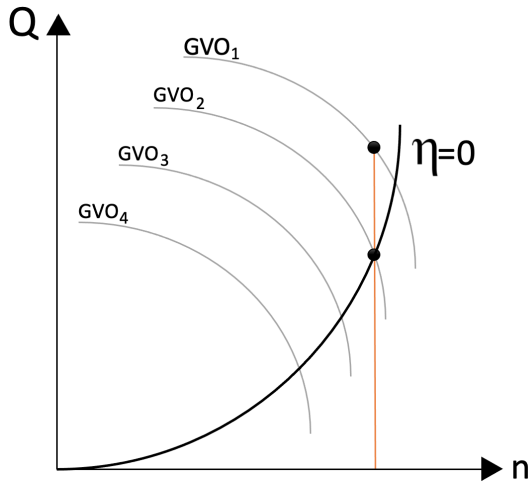
Figure 3.1: Efficiency curve for a decreased flow Q, a constant rotational speed n, and different guide vane openings.

The theory in the present section is mainly based on high head Francis turbine theory, commonly lectured at the Waterpower Laboratory. It concerns a traditional assembly of a Francis turbine, meaning a runner, a set of guide vanes, a set of stay vanes, a spiral casing, and a draft tube. Given that the current design does not include a spiral casing or conventional stay vanes, and considering that the entire unit is designed for low-head conditions, certain exceptions are taken into consideration. These will be presented and discussed alongside the theoretical framework.

---

[4]Personal conversation with Storli [30]

3.2.1 Runner

The present subsection is divided into two main parts: main dimensions and blade geometry. All theory is based on the assumption of infinitely thin blades until the thickness is calculat.

Main dimensions

When designing the runner certain constraints are given. n is chosen to be 1000 rpm[5]. The inlet diameter, D_1, is given as 0.54 m from the stay vane outlet diameter. These considerations affect the methodology for calculating the main dimensions as described below.

Unless otherwise is stated, the theory presented in the current section is based on "Pumper & Turbiner" by Brekke [27].

The hydraulic parameters H and Q, together with a set of values from empiricism based on both economical and practical considerations, create the base for deciding the runner's main dimensions. The turbine is designed at the best efficiency point (BEP).
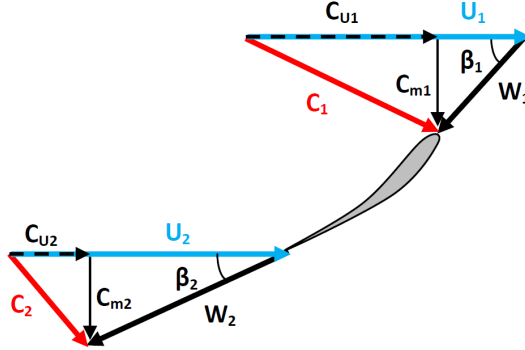
Figure 3.2: Velocity triangles at the inlet and outlet of a runner, decomposed in the peripheral, absolute, and relative direction. [1]

It is common to decompose the velocity in a peripheral, absolute, and relative direction as illustrated in Figure 3.2. The absolute velocity c is decomposed into the meridional velocity component c_m following the streamline, and the peripheral component c_u. The variables u and w represent

---

[5]Used in the project work of Lund [31]

the peripheral and relative velocities, respectively. Lastly, the blade angle is defined as β.

Outlet dimensions

When designing the runner outlet dimensions, the goal is to utilize all the kinetic energy in the runner, and thus have irrotational flow at the outlet. This is assumed by setting $c_{u2} \approx 0$.

According to Brekke β_2 and u_2 are usually within the intervals in Table 3.2. In the case of a low head Francis turbine, it is typical to have a larger value for β_2 and a smaller value for u_2.

Table 3.2: Reference turbine data

$$
\begin{array}{ccc}
15° & < \beta_2 < & 22° \\
35 \text{ m/s} & < u_2 < & 42 \text{ m/s}
\end{array}
$$

As c_{u2} is assumed zero it implies that c_2 is equal to its meridional component c_{m2}, as Equation (3.3) describes.

$$c_2 = c_{m2} = u_2 \cdot tan(\beta_2) \tag{3.3}$$

Due to the curvature in the channel c_{m2} will experience slightly different values at the hub and shroud. An average value for c_{m2} is calculated, and as a consequence, the outlet angle at the hub and shroud will be too large and too small, respectively.

Derived from the continuity equation, the outlet diameter is D_2 found using Equation (3.4). n can be calculated using Equation (3.5).

$$D_2 = \sqrt{\frac{4 \cdot Q}{\pi \cdot c_{m2}}} \tag{3.4}$$

$$n = \frac{u_2 \cdot 60}{\pi \cdot D_2} \tag{3.5}$$

Framo employs an asynchronous motor, meaning that the rotational speed will deviate from n with a slip range of 6 to 10 rpm [32]. To compensate for this, the slip is added to the rotational speed when dimensioning the runner.

Cavitation control

Cavitation is a highly complex flow phenomenon that may occur in lower-pressure regions during turbine operations [27]. Its presence can cause detrimental effects such as pitting, erosion, noise, and vibrations and lead to performance losses. Cavitation arises in areas where the pressure is below the vapor pressure. The risk can be reduced by either increasing the runner dimension or submerging the turbine. To check if cavitation is likely to occur the theory for calculating the required submergence is given below. It assumes sediment-free water and a safety margin should be added if the turbine is operated in silty water [33].

The net positive suction head $NPSH_r$ is calculated using Equation (3.6). It uses the speed number Ω which is a non-dimensional variable used to classify and compare different turbine designs. Ω is found using Equation (3.7).

$$NPSH_r = a\frac{c_{m2}^2}{2g} + b\frac{u_2^2}{2g} \tag{3.6}$$

$$\Omega = \underline{\omega} \cdot \sqrt{\underline{^*Q}} \tag{3.7}$$

$^*Q$ denotes flow at BEP and the underscore indicates that reduced values are used, meaning that they are divided by $\sqrt{2gH}$. The relation between the empirical parameters a and b, and Ω is presented in Table 3.3.

Table 3.3: Correspondence between Ω, a and b

	a	b
$\Omega < 0.55$	1.12	0.055
$\Omega > 0.55$	1.12	$0.1 \cdot \Omega$

The required submergence H_s is derived from the Energy Equation between the runner outlet and the tailwater, given in Equation (3.8).

$$H_s = h_{atm} - h_{va} - NPSH_r \tag{3.8}$$

h_{va} denotes the vapor pressure at the runner outlet and h_{atm} is the atmospheric pressure at the tailwater level. At sea level, h_{atm} is 10.3 m

and h_{va} is 0.125 m at 10°. A negative H_s implies that the turbine should be located below the tailwater level. If installed above H_s the pressure at the runner outlet may drop below the vapor pressure and lead to cavitation. Likewise, if installed below H_s the runner will have a safety margin against cavitation. As the submergence is calculated for $^*Q$ the corresponding H_s will not be sufficient if the turbine is run for a flow above $^*Q$. This is not relevant for the turbine discussed in this thesis, which will rather experience a decrease in flow.

Inlet dimensions

When designing the inlet dimensions, the angles should correspond to BEP. The Euler turbine equation is used to find the hydraulic efficiency η_h and is presented in Equation (3.9).

$$\eta_h = \frac{u_1 c_{u1} - u_2 c_{u2}}{gH} \approx 2\underline{c}_{u1}\underline{u}_1 \qquad (3.9)$$

As the flow is assumed irrotational, the last term is neglected. The hydraulic efficiency is often assumed to be 0.96, only accounting for friction losses in the runner.

As mentioned above, turbines are categorized as impulse and reaction turbines. This can mathematically be described by the reaction ratio, R, presented in Equation (3.10). R is defined as the static pressure drop between the rotor and stage.

$$R = 2\underline{c}_{u_1}\underline{u}_1 - \underline{c}_{u_1}^2 \qquad (3.10)$$

$\underline{u}_1$ is usually between 0.7 to 0.75 based on having a reaction ratio of 0.5 to 0.55 for a Francis turbine [2]. From this $\underline{c}_{u1}$ can be found rearranging Equation (3.9). From the tip speed ratio, D_1 is found using Equation (3.11).

$$D_1 = \frac{2\underline{u}_1}{\underline{\omega}} \qquad (3.11)$$

To avoid retardation of flow an acceleration factor K_{accel} in the range of 1.1 to 1.5 of the c_m component is chosen [34]. From continuity and the different expressions for the inlet and outlet area, an expression for the inlet height B_1 is given in (3.12).

$$B_1 = \frac{K_{accel} \cdot D_2^2}{4 \cdot D_1} \tag{3.12}$$

The blade inlet angle β_1 is found from Equation (3.13).

$$\beta_1 = \arctan\left(\frac{c_{m1}}{u_1 - c_{u1}}\right) \tag{3.13}$$

Brekke [35] states that the angle between c_1 and w_1 should be close to $90°$. As D_1 and n are given the inlet and outlet conditions are calculated by rearranging the equations stated above. The resulting main dimensions are chosen based on getting values close to or within the empirical ranges and observing the angle between c_1 and w_1. To do this, a Matlab script given in section B.1 is used.

Blade geometry

As the main dimensions are found, the runner blade profile is to be considered. To achieve this, the runner is evaluated from three perspectives: an axial, radial, and a 3D view. The following theory is mainly from Eltvik et. al [2] and the remaining sources are introduced in a sequential manner.

Axial view

The axial view is constructed by defining equally distributed streamlines between the hub and shroud. Throughout the runner, streamlines follow the velocity distribution, where higher density indicates higher velocity. As illustrated in Figure 3.3, the shape can be circular or elliptic, depending on the parameters a and b. a is related to the difference between D_1 and D_2, while b depends on the hub height. The hub height is found by multiplying the outlet diameter D_2 with a factor between 0.4 and 0.6 [36].

The first streamline is defined at the shroud and given in Equation (3.14),

$$S = \int_{-k}^{0} \sqrt{1 + (\frac{dy}{dx}^2)}dx \tag{3.14}$$

where $k = R_1 - R_2$ and the ratio $\frac{dy}{dx}$ is derived from the standard elliptic function presented in Equation (3.15).
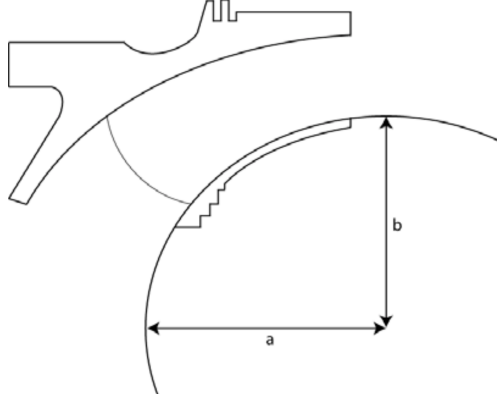
Figure 3.3: An elliptic approximation for the runner. [2]

$$\frac{dy}{dx} = \frac{b}{2\sqrt{1 - (\frac{x}{a})^2}} \left(-\frac{2x}{a^2} \right) \tag{3.15}$$

After determining the number of streamlines j, the remaining streamlines are calculated from the first, assuming equal flow distribution. Each streamline is divided into a number of points i, equally distributed. A point $(i, j+1)$ is calculated from the prior streamline by the normal line $b_{i,j}$ to the line made up by the adjacent points $(i-1,j)$ and $(i+1,j)$. This is illustrated in Figure 3.4.

The coordinates Z and R are derived in [1] and presented in Equation (3.16) and (3.17), respectively.

$$Z_{i,j+1} = Z_{i,j} - b_{i,j} \cdot cos(\alpha_{i,j}) \tag{3.16}$$

$$R_{i,j+1} = \sqrt{R_{i,j}^2 + \frac{A_{i,j}\sin\alpha_{i,j}}{\pi}} \tag{3.17}$$

$A_{i,j}$ is the inflow area, and $\alpha_{i,j}$ is found through Equation (3.18).

$$\alpha_{i,j} = \arctan\left(\frac{Z_{i-1,j} - Z_{i+1,j}}{R_{i-1} - R_{i+1,j}} \right) \tag{3.18}$$

17
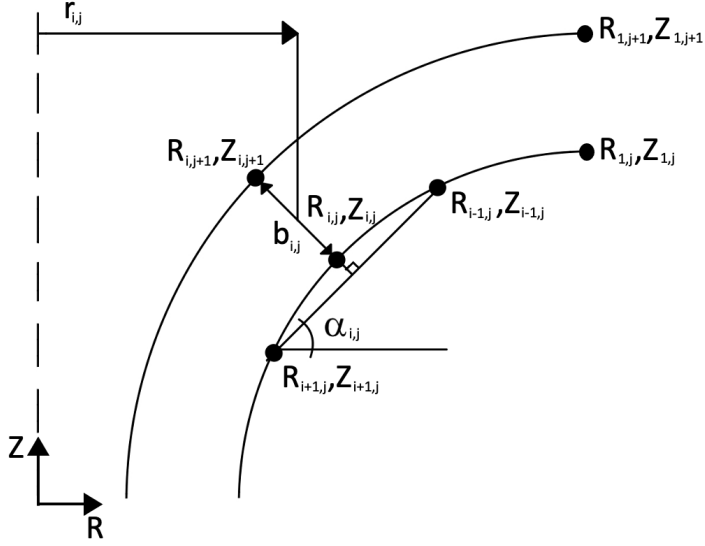
Figure 3.4: Streamline approach to the following point $(i, j+1)$

Energy distribution

The energy distribution describes how the potential and kinetic energy is transferred into rotational energy along the blade and is assumed equal for all streamlines. It is defined by choosing a $u \cdot c_u$ distribution that is zero at the outlet, assuming irrotational flow. It is desirable to have a small slip angle at the outlet to avoid cavitation due to large pressure differences between the pressure and suction side [2]. u depends on the radius and the angular velocity and is therefore known for all points. c_u can be calculated from u and $u \cdot c_u$ for all points. c_m is assumed to accelerate linearly according to the acceleration factor K_{accel}. From this, the blade angle distribution β is calculated using Equation (3.13).

Radial view and G-H plane

To get a 3D view of the runner a radial view needs to be constructed. The transformation from an axial view to a radial view is done using a G-H plane. G and H represent the length of a streamline in the axial and radial planes, respectively. G is found using Equation (3.19) and has a starting point equal to zero.

18

$$G_{i,1} = G_{i-1,1} + \sqrt{\left(R_{i-1,1} - R_{i,1}\right)^2 + \left(Z_{i-1,1} - Z_{i,1}\right)^2} \qquad (3.19)$$

H is found from the blade angle β and G by using Equation (3.20).

$$\Delta H = \frac{\Delta G}{tan\beta} \qquad (3.20)$$

The radial view is then obtained by introducing polar coordinates as Equation (3.21)[6].

$$\Delta\theta = \frac{\Delta H}{R} \qquad (3.21)$$

By using coordinates from the axial and radial plane, 3D plots can be made by transforming the polar coordinates into cartesian again. This creates 3D models of the blade and the total runner.

Runner blade thickness

To withstand dynamic pressure pulsations in the runner and pressure difference between the blades, a certain blade thickness t must be added. This would ideally be derived from a complete stress analysis. However, as the geometry tends to be quite complex, a conservative estimate is done using a simplified stress analysis. The estimate should be validated through a full Final Element Method (FEM) analysis of the blade, which is outside the scope of this thesis.

Assuming that the hub is considered rigid compared to the shroud, it is applicable to perform a simplified stress analysis by representing the blade as a straight beam from the hub to the shroud. Figure 3.5 illustrates this model with an equally distributed load, $q = \Delta r \Delta p$. The pressure difference along the blade Δp and the radial length Δr is assumed constant. The corresponding bending moment M is governed by Equation (3.22).

---

[6]Only valid for smaller values of ΔH [1]
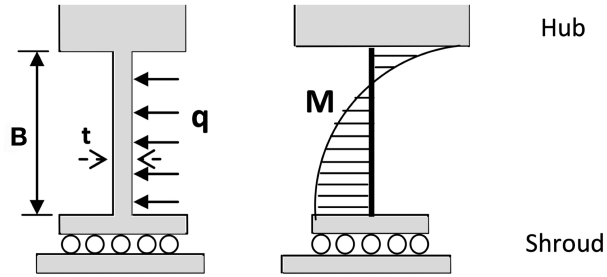
Figure 3.5: Clamped-guided beam with equally distributed load (left) and related bending moment (right). [1]

$$M = q\frac{B^2}{3} \tag{3.22}$$

The maximum bending stress σ_{max} and the moment of inertia I are given by Equation 3.23 and 3.24, respectively.

$$\sigma_{max} = \frac{M}{I}\frac{t}{2} \tag{3.23}$$

$$I = \frac{\Delta r \cdot t^3}{12} \tag{3.24}$$

The lengths Δr, L, and B are defined as Figure 3.6 illustrates.
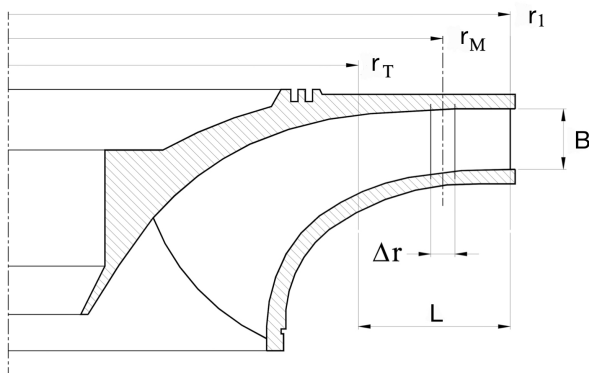
Figure 3.6: Definition of L, r_m and Δr. [1]

The minimum blade thickness t_{min} at the trailing edge is found by rearranging Equation (3.22)-(3.24) and is presented in Equation 3.25.

$$t_{\min} = \sqrt{\frac{2 \cdot B^2 \cdot \Delta p}{\sigma_{\max}}} \tag{3.25}$$

The pressure difference Δp is found by studying the torque on the runner M_{runner}. By assuming that the torque is fully transferred from the flow to the blade, it is defined as the ratio between power and angular velocity, as in Equation (3.26). The final pressure difference is given by Equation (3.27).

$$M_{\mathrm{runner}} = Z_r \cdot L \cdot B \cdot r_M \cdot \Delta p = \frac{P}{\omega} \tag{3.26}$$

$$\Delta p = \frac{P}{Z_r \cdot L \cdot B \cdot r_M \cdot \omega} \tag{3.27}$$

Z_r denotes the number of runner blades, while r_M is the mean radius between the inlet radius r_1 and the radius where the torque ends r_T. Using this method gave a blade thickness of 24 mm, which compared to similar-sized turbines [37] is unrealistically thick. Consequently, a thickness of 5 mm was chosen[7].

As the blade thickness is added, the shape of the trailing edge has to be considered. The shape can influence the flow pattern, causing undesirable phenomena such as vortex shedding and additional noise in the wake [2]. Having a design where the leading edge is rounded and a trailing edge with an angle of 30° has proved good to minimize the occurrence of vortex shedding. However, the more optimal the shape is with respect to vortex shedding, the higher the velocity will be and thereby give an increased possibility of cavitation[8]. A design with a 60° "cut-off" shape was selected as a compromise. When it comes to the leading edge design, a rounded shape is typically considered the standard choice.

A modified Matlab script adapted by Wei Zhao [2] uses the theory described here to make axial, radial, and 3D plots. It also produces information about the blade curvature and thickness that are used when making a 3D model of the runner in Ansys BladeGen. From this, the flow path of the runner is created with a hexahedra mesh using Ansys TurboGrid.

---

[7]Personal conversation with Vangdal [32].
[8]Personal conversation with Trivedi [23]

Number of blades

When determining the number of runner blades, it is important to have a sufficient number to prevent backflow.
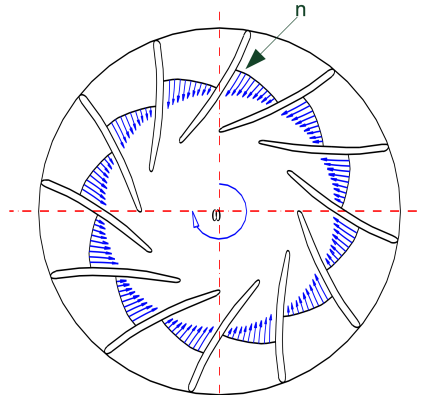
Figure 3.7: The relative velocity distribution along the channel. [1]

An initial number of blades is guessed before calculating the flow through each blade channel, as illustrated im Figure 3.7. A value for w at the suction side is chosen before the distribution is calculated for the width of the channel down to the pressure side of the next blade. Here the velocity is at its lowest, and to avoid backflow this value must be positive. The expression used to calculate the change in w is given in Equation (3.28) [34].

$$\frac{\partial w}{\partial n} = -2\omega - \frac{w}{r} \tag{3.28}$$

n is the width of the channel and is found based on the number of blades chosen, including the blade thickness, while r is the radius. With this expression and the inlet angle β_1, the velocity in the streamline direction c_m is calculated so that the flow through each section Q_{sec} can be found using Equation (3.29),

$$Q_{sec} = \iint c_m \partial A \tag{3.29}$$

where A is the inflow area. Multiplying Q_{sec} with the number of blades results in the total flow, and if this value is bigger than the given flow Q no

backflow will occur. If not, the number of blades should be increased [1]. For this design, the number of blades is calculated as described here using a Matlab script given in section B.1.

3.2.2 Stay vanes

Conventionally stay vanes are mounted at the outlet of the spiral casing to help withstand the hydraulic forces acting on the casing. The stay vanes are then designed to give as little friction losses as possible after both runner and guide vanes have been designed. However, the design presented in this thesis deviates from conventional approaches and is based on a reference design (Figure A.2) developed by Framo. In this design, water enters the stay vanes in the gravitational direction, and exits radially towards the runner. In the reference design, the leading edge has a 72° angle of attack, while the trailing edge is 43°[9]. Additionally, the design has a minimum inner diameter of 0.8 m at the inlet and 11 vanes. The shape of the leading and trailing edges follow the same arguments as for the runner blade.

Based on the findings from Lund's project [31], a design is developed where the leading edge is aligned with the freestream velocity, while the trailing edge remains unchanged. This was found to omit negative pressure in the component. Additionally, the reference design had a 90° bend between the stay vanes and guide vanes. It was anticipated to cause excessive cavitation and separation due to the small radius of curvature. Hence, a second geometry with an increased radius of curvature was proposed[10]. Both versions were created using Ansys BladeGen and meshed with tetrahedral elements in TurboGrid.

3.2.3 Guide vanes

Guide vanes are used to control the flow through the runner by adjusting the opening angle and thus the inlet angle to the runner. This gives a more flexible operational window for the turbine. The water will also get accelerated throughout the guide vanes by increasing the c_u component.

From conversations with Vangdal [32] certain values for guide vane design are set. As the stay vanes and runner are calculated prior, the space available for the guide vanes is determined to be 110 mm. The number of guide vanes is 24 and the NACA 30 is chosen as the guide vane shape. Ansys SpaceClaim

---

[9]Personal conversation with Vangdal [32]
[10]Personal conversation with Storli [30]

is used to make the guide vane model before it is meshed in Ansys Mesh.

The number of guide vanes can if chosen poorly lead to pressure pulsations when the runner blades pass. To minimize this risk, the number of guide vanes Z_{gv} must conform with Equation (3.30).

$$\frac{Z_{gv}}{Z_r} \neq Integer \tag{3.30}$$

Positioning and shape

The guide vane rotational center D_0 can be found by multiplying D_1 by a factor between 1.15 and 1.26 [38]. D_0 is usually located in a place between the center and three-quarters towards the trailing edge. Figure 3.8 display the relation between these variables. The length from the guide vane outlet diameter D_{gvo} and D_0 is denoted L_0, and is dependent on Z_{gv} to assure that the vanes overlap in the closed position and thereby avoid full rotation. If the guide vanes function as a closing mechanism, an overlap of 10-15% is necessary. Having fewer and longer guide vanes will lead and accelerate the water better, but also induce more friction losses. Having more and shorter vanes reduce friction losses but will give less acceleration to the water into the runner. The shape can either be a symmetrical profile like the NACA profiles or asymmetric around the camber line [2].
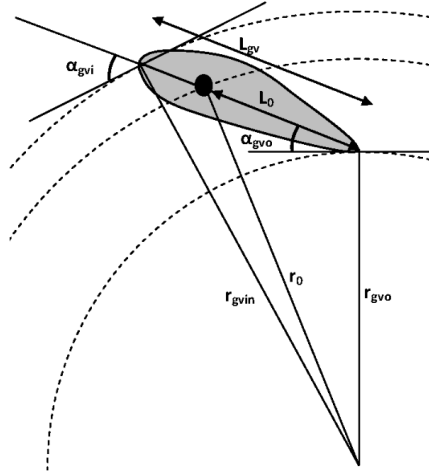
Figure 3.8: Guide vane geometry. [1]

The vane length L_{gv} was iteratively determined and based on D_{gvo} and ensuring sufficient space between the guide vane's inlet diameter and the stay vane's outlet diameter.

Guide vane outlet

To ensure that the guide vanes are not affected by the runner flow, D_{gvo} is set to be 5% greater than D_1. This gap will also be affected by the guide vane opening, and when fully opened the gap will be smaller. Assuming that the gap is sufficient so that no energy is lost, free vortex theory can be used [2], and thus Equation (3.31) is applied.

$$c_{u1} \cdot r_1 = c_{u,gvo} \cdot r_{gvo} \tag{3.31}$$

The meridional component $c_{m,gvo}$ is found through continuity, and the outlet angle α_{gvo} is found by use of the velocity triangle. This is presented in Equation (3.32) and (3.33), respectively.

$$c_{m,gvo} = \frac{Q}{2\pi \cdot B_1 \cdot r_{gvo}} \tag{3.32}$$

$$\alpha_{gvo} = \arctan\left(\frac{c_{m,gvo}}{c_{u,gvo}}\right) \tag{3.33}$$

Guide vane inlet

Conventionally, the design process of a complete Francis unit starts at the runner and moves outwards meaning the guide vanes, stay vanes, and finally the spiral casing. In this case, due to the bend between the stay vanes and guide vanes, the conservation of spin is satisfied by calculating the inlet angle of the guide vanes based on information from the trailing edge of the stay vanes. The requirement is governed by Equation 3.34, where K_i denotes a constant value to its respective radius. As Figure 3.9 represents, the radius decreases for the different streamlines from 1 to n. Since each streamline has the same shape and a gradually decreased radius, a linear correlation from hub to shroud is assumed. Hence, only streamline 1 and n are considered.

$$c_u \cdot r_i = K_i \tag{3.34}$$

As K_1 and K_n are identified, it is possible to calculate the peripheral component of the velocity at the shroud and hub, respectively. The merid-
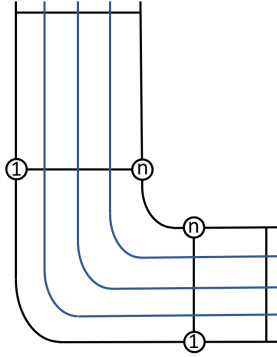
Figure 3.9: Streamlines between stay vanes and guide vanes. Streamline 1 and n denote the shroud and hub, respectively.

ional component at the inlet, $c_{m,gvi}$ is found from the continuity equation, using the inlet area of the stay vane inlet. Finally, the inlet angles $\alpha_{gvi,j=1,n}$ are found from the relation in Equation (3.35).

$$\alpha_{gvij=1,n} = \arctan\left(\frac{c_{m,gvi}}{c_{u,gvij=1,n}}\right) \tag{3.35}$$

Initially, a design (depicted in Appendix F) was created based on the calculated $\alpha_{gvi,j=1,n}$. However, Ansys Mesh encountered difficulties in meshing the asymmetric design. Algorithms like Sweep and MultiZone were not used as they are unable to generate a mesh of an asymmetric cross-section. Hence, the Hex Dominant method was attempted. Despite being combined with tetrahedrons, even the coarsest element size, 1E-4, generated a mesh too expensive and accurate for this purpose. Consequently, a set of symmetric guide vanes were created with an inlet angle equal to the mean value of the two angles. This was meshed with the default in Ansys Mesh, combining both hexahedral elements and wedges.

Guide vane openings

To see if the introduction of guide vanes can compensate for bad efficiency when reducing the flow, simulations are run with the reduced flow for a smaller GVO. From Framo the flow is reduced gradually down to $^*Q \cdot 0.5$ [3]. This gives an equal reduction of the c_{m1} and a reduced inlet angle α_1, illustrated in Figure 3.10. It is assumed that β_1 is kept constant as it provides

Figure 3.10: Inlet triangle for a reduced flow.

a no-slip angle when the water hit the runner.

Simulations are performed for $^*Q$, $^*Q \cdot 0.5$, and $^*Q \cdot 0.75$ with GVOs corresponding to the flow. To plot the trend with reduced flow three different angles are simulated for.

3.2.4 Draft tube

The overall performance of a reaction turbine can be elevated by implementing a draft tube [2]. The purpose of the component is to convert the kinetic energy at the turbine outlet into pressure energy in a way that avoids flow separation. This is assured by increasing the cross-section area towards the outlet. Its presence enables backflow control as it increases the pressure head at the runner exit.

The present project will only concern a draft tube cone as the whole unit is located beneath tailwater. The component has a circular shape and is directly coupled to the turbine outlet. Hence the inlet diameter of the draft tube cone $D_{c,1}$ is equal to D_2. $D_{c,2}$ is dependent on the cone length L_c and is presented in Equation 3.36. To avoid separation of flow the angle between the center line and the wall γ is kept below $3°$ [2].

$$D_{c,2} = D_{c,1} + 2 \cdot L_c \cdot tan(\gamma) \tag{3.36}$$

In this project, a simple draft tube is constructed for simulation purposes. As a simplification, L_c is assumed to be around twice the outlet

diameter[11]. A 3D model was made using Ansys SpaceClaim, before a coarse mesh was made with the default method in Ansys Mesh, combining both hexahedral elements and wedges. A coarse mesh is used as studying the flow characteristics here is not the focal point in this thesis.

---

[11]Personal conversation with Trivedi [23]

Results and discussions

The following chapter is divided into three main sections; final geometry, verification of the computational model, and lastly CFD results. The results will be presented and discussed along the way.

4.1 Final geometry

The resulting geometry for each component is presented in this section, in the same order as the theory was presented in section 3.2.

4.1.1 Runner

The main dimensions were calculated using the Matlab script in section B.2 and the final results are presented in Table 4.1. The acceleration factor, K_{accel}, was determined to be 10%, while Ω and R were calculated to be 0.83 and 0.63, respectively. Figure 4.1 presents the axial view of the runner. The constants a and b in subsubsection 3.2.1 were determined to be 0.07 and 0.45·D_2, respectively. The streamlines close to the shroud are closer together than at the hub, indicating a higher velocity here.

Table 4.1: Resulting main dimensions for the inlet and outlet of the runner.

	Variable	Value	Unit
Outlet	D_2	47	cm
	β_2	30	°
	u_2	25	m/s
Inlet	D_1	54	cm
	B_1	11.3	cm
	β_1	56	°
	α_1	34	°
	u_1	29	m/s
	H_s	-4.3	m
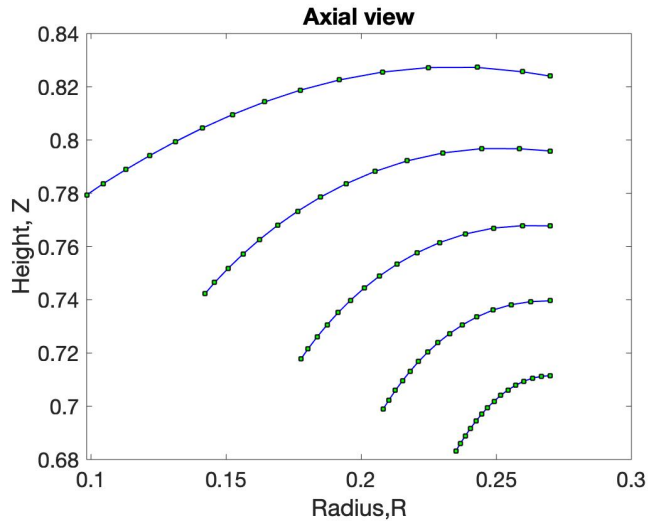
Figure 4.1: Axial view of the runner displayed by 5 streamlines with 15 points on each streamline.

The energy distribution plotted for the shroud and hub is presented in Figure 4.2 and Figure 4.3, respectively. The chosen $u \cdot c_u$ distribution ensures that the c_u component is zero at the outlet, establishing irrotational outlet conditions. The c_m component is assumed to accelerate linearly based on K_{accel}. u decreases throughout the blade, coinciding with the values obtained in Table 4.1. The decrease is more prominent at the hub, coinciding with the expectation that the velocity is higher closer to the shroud, as streamlines are closer together here.
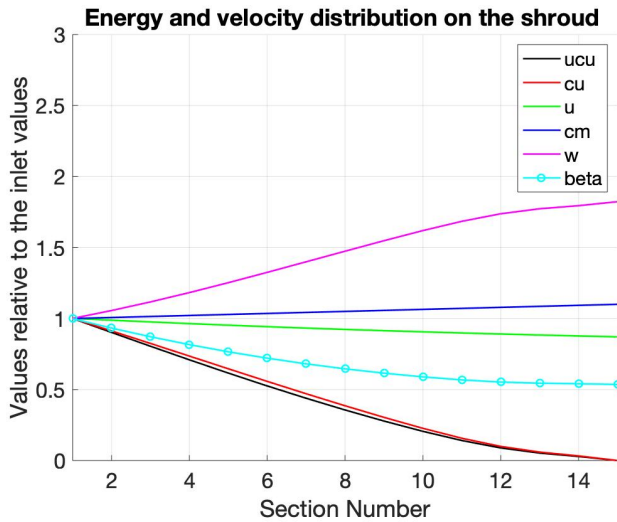

Figure 4.2: Normalized energy distribution plotted along the shroud.

There is a slight increase in β at the hub before it decreases towards the outlet. This behavior may be caused by the fact that $u - c_u$ becomes negative between section 3 and 7. This increase in β results in a slightly reduced w distribution, which is undesired as it increases the possibility of backflow through the runner. This can be an indication that the chosen $u \cdot c_u$ is not optimal for this current design, and should be changed. Plots of the G-H plane and a final 3D view of the runner using the Matlab script in section B.4 are presented in Appendix D. The calculated runner blade thickness was considered too conservative for its purpose, and a final thickness of 5 mm was chosen instead. Hence, this should be further investigated. The leading and trailing edge was given a round and cut-off shape, respectively.

31
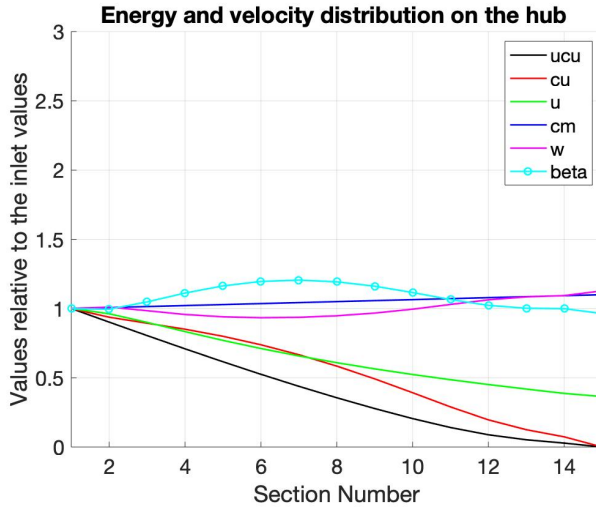
Figure 4.3: Normalized energy distribution plotted along the hub.

Using the Matlab script in section B.1, the number of runner blades was calculated to be 11. The result is based on an initial relative velocity at the suction side of 37 m/s, which is found from the outlet velocity triangle. If the simulations reveal a relative velocity at the suction side below the threshold, increasing the number is necessary to avoid backflow. Based on the results above, the final runner geometry is presented in Figure 4.4.
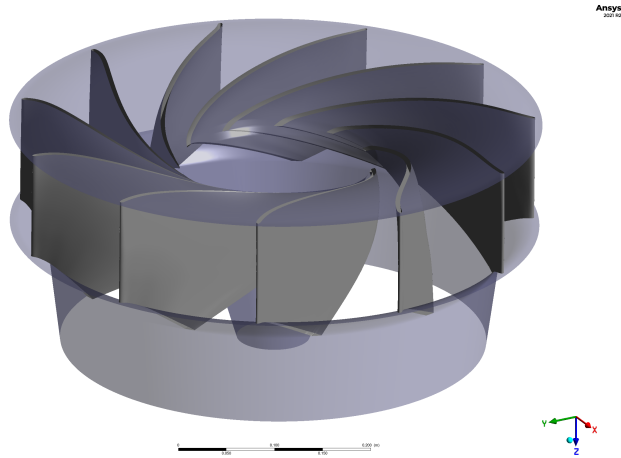
Figure 4.4: A 3D model of the final runner design created in Ansys BladeGen.

4.1.2 Stay vanes

The meridional view of the two different stay vane outlet designs is constructed based on the arguments in subsection 3.2.2. While the stay vanes remain unchanged in both designs, there are variations in the transition between the stay vanes and the guide vanes. This is illustrated in Figure Figure 4.5.
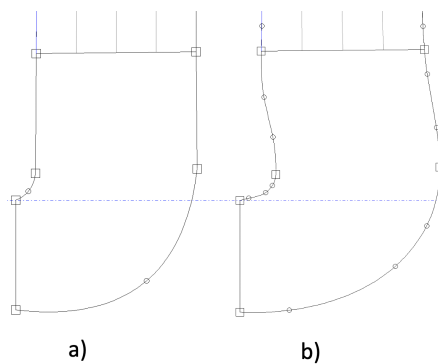
Figure 4.5: Meridional view of the stay vane outlet designs where a) is the base case and b) is the new design.

4.1.3 Guide vanes

A summary of the key guide vane variables is given in Table 4.2.

Table 4.2: Key guide vane parameters

Variable	Value	Unit
Z_{gv}	24	-
L_{gv}	0.13	m
D_{gvo}	0.567	m
D_0	0.648	m
α_{gvi}	58.5	°
α_{gvo}	33.5	°

D_0 was found by multiplying D_1 with 1.2, while the guide vane length was 0.13 m. It was later discovered that the combination of cord length and the number of vanes resulted in an overlap of ca. 50% in a closed position. An improved approach would involve reducing the number of guide vanes while maintaining the same length. The adjustment will lead to a reduced overlap while still preventing the vanes from completing a full rotation. Additionally, fewer guide vanes will reduce friction losses. Due to the late discovery of this issue, these modifications were not implemented. Figure 4.6 shows the resulting guide vane mesh.
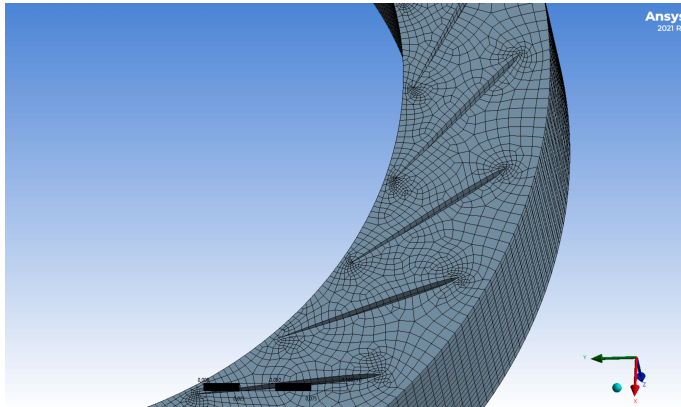

Figure 4.6: A section of the meshed flow path of the guide vanes.

4.1.4   Draft tube

The length of the draft tube is set to 1 m, based on the argument stated in subsection 3.2.4. Using Equation (3.36), $D_{c,2}$ was found to be 0.575 m.

4.2   Verification of the computational model

4.2.1   Grid independence study

Based on the finest refinement allowed in Ansys TurboGrid due to computational memory, a simplified convergence study explained in subsection 3.1.3 was conducted. It is important to note that the study was conducted before discovering that the curvature of the runner blades was reversed. However, due to time constraints, the result was considered satisfactory for its purpose.

Table G.1 in Appendix G displays the number of elements for each component and the overall assembly for all refinements. Everything but the element size was kept constant when refining the mesh. Decisions regarding the mesh setup are derived from the theory discussed in subsection 3.1.2. The near-wall element size was chosen as absolute, meaning the investigated parameter had to remain unaffected by variations in the near-wall region. Hence, the pressure at the runner outlet was examined. As can be seen in Figure 4.7, the pressure stabilizes between the last two refinements. Thus, the second last refinement, with $2.05 \cdot 10^6$ elements, is considered sufficient.

4.2.2   Residuals

A residual target was set to 1E-4 with 500 iterations of time step 0.01. The simulations did not reach this target by the end of the iterations. However the change between the 10 last iterations was investigated, showing that the values had converged as the change was insignificant between them. The residuals for the base case are given in Figure G.1.
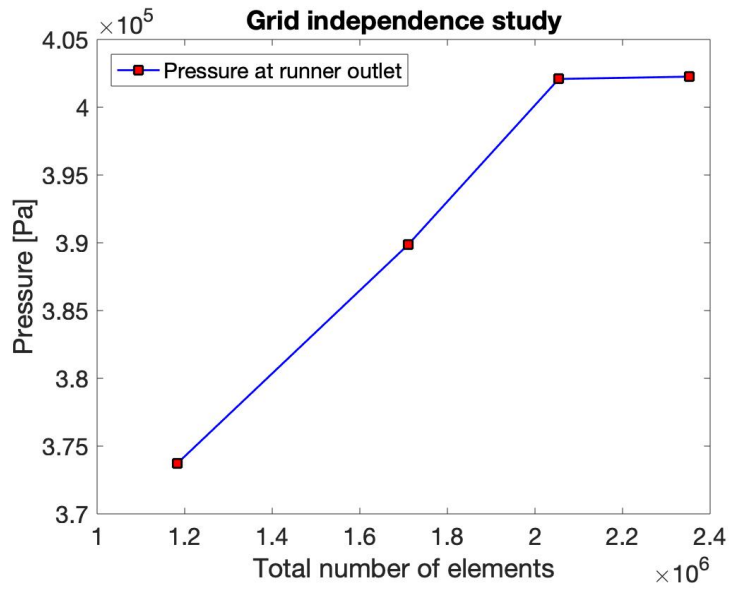
Figure 4.7: Grid independence study done for four different element sizes.

4.3 CFD results

Pursuing the theory presented in section 3.1, all assumptions from Table 3.1 are considered in Ansys CFX Pre. An illustration of the final, complete assembly is depicted in Figure 4.8.
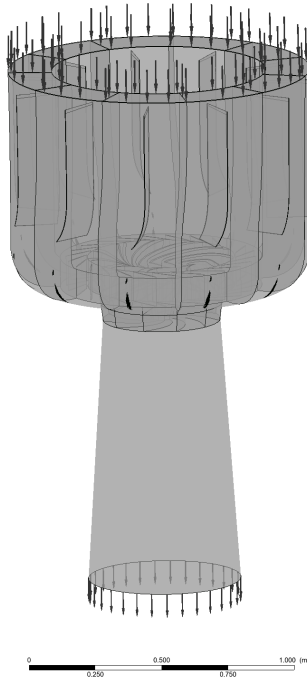
Figure 4.8: A complete view of the unit, depicted in Ansys Pre.

4.3.1 Base case

The base case is the turbine designed for BEP and is simulated for $^*Q = 2.5$ m^3/s. When the results for the different components are discussed, is it done in the same order as the flow direction.

4.3.2 Stay vanes

As the head is applied as an inlet condition to the turbine, no negative pressure is present in the stay vanes. In Figure 4.9 the velocity vectors at the

trailing edge of the stay vanes are displayed. It can be seen that the induced spin ceases before entering the guide vanes. When looking into the cause of this, it was discovered that the length of the stay vanes deviated from the reference design. The present design has a gap of 15 cm between the stay vanes and the guide vane hub. A reduction of the gap would maintain the spin further down. Another solution could be to start curving the stay vane further upstream. This is predicted to smoothly guide the water into a rotational spin, while still keeping the same outlet angle. Furthermore, Figure 4.9 reveals that the flow in the middle region between the vanes is almost unaffected by the change in direction. Increasing the number of stay vanes would presumably change the flow direction and accelerate the flow better.
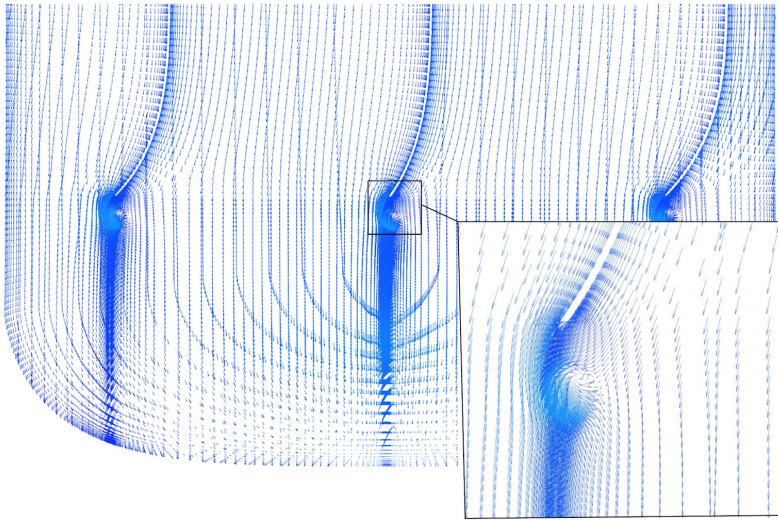

Figure 4.9: Velocity vectors around the stay vanes.

The lack of induced spin may describe why the second stay vane outlet geometry had little effect on the efficiency, only increasing it by 0.01%. However, when achieving better overall performance in the stay vane, this design should be further investigated by running a new simulation.

4.3.3 Guide vanes

As the stay vanes fail to induce a significant spin, the water is observed to enter the guide vanes radially inwards. Consequently, high pressure is built up at the pressure side of the guide vanes, while a wake of negative pressure arises at the suction side. This can be seen in Figure 4.10, where the velocity contour between the guide vanes is presented. The velocity accelerating near the leading edge on the suction side indicates the separation of flow, which increases the chance of bubbles forming. A decreased angle of attack would reduce the area of impact and thus reduce losses.
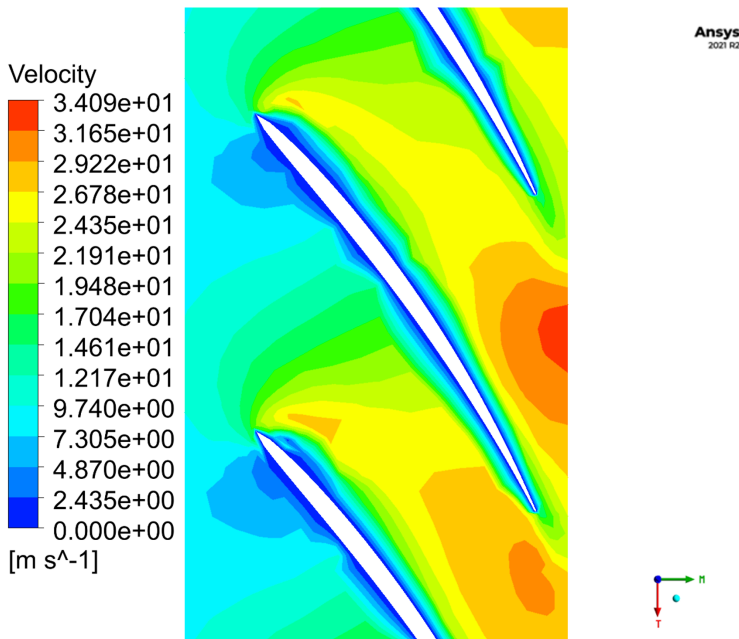
Figure 4.10: A contour plot of the velocity around the guide vanes, shown midway between the hud and shroud. The pressure side is located on the left, while the suction side is positioned on the right.

Due to the conservation of spin, the velocity will be higher at the shroud than at the hub, enlarging the risk of bubbles forming here, and thereby cavitation. As explained in subsection 4.1.3, the initial guide vane design with an asymmetric leading edge had to be simplified by using a symmetric
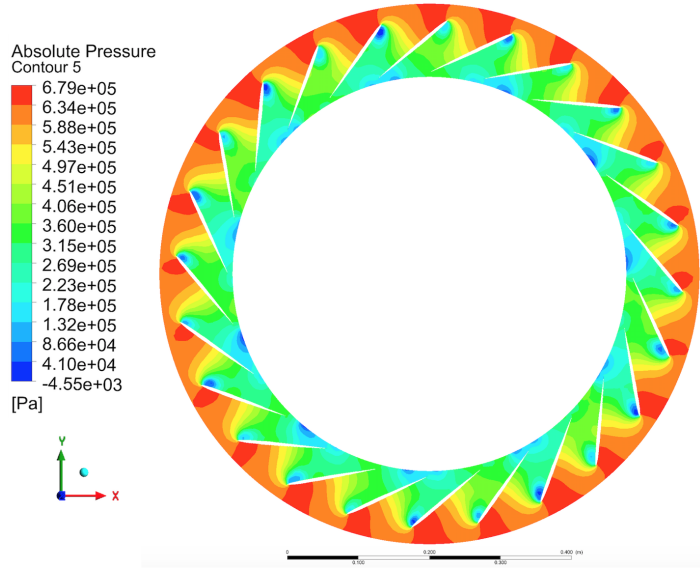
Figure 4.11: Absolute pressure at the guide vanes, shown midway between hub and shroud.

design instead. It is likely that this initial design would have accounted for the low-pressure regions occurring at the shroud.

As can be observed in Figure 4.11 there is a pattern where almost every other guide vane reaches a lower pressure at the suction side. This is likely related to having 24 guide vanes and 11 stay vanes, which also applies to the relation between Z_{rb} and Z_{gv}. Following the reasoning from subsection 4.1.3, having fewer guide vanes would likely hinder these patterns from forming, and lead to a more equal load distribution on the vanes.

Runner

Figure 4.12 reveals that the entire suction side of the blade experience negative pressure, with higher magnitudes concentrated near the shroud and the leading edge. The pressure side is dominated by negative pressure at the trailing edge towards the shroud. According to the high-head Francis theory the leading edge share the same angle between the hub and shroud. However, as described in chapter 2, Ayli et. al concluded that a lean angle of a maximum of 10 degrees from the shroud in any direction could withstand

40

the occurrence. Due to time constraints, this was not investigated. This negative pressure may also be caused by the suboptimal inlet conditions caused by the stay vanes.
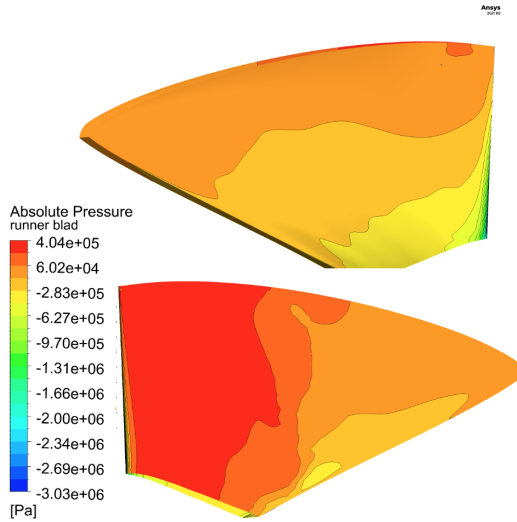
Figure 4.12: Absolute pressure at the suction side (top) and pressure side (bottom).

From looking at Figure 4.13 the flow from the guide vanes is directed towards the runner blades close to the leading edge. This leads to an acceleration of flow around the leading edge, where the flow reaches very high velocities, highlighted in Figure 4.13. An explanation for this may be the leading edge design, contributing to a lot of separation of the suction side. This reduces the efficiency as this leaves less flow left to rotate the blades. It can also indicate that the angle between the guide vane outlet and the runner inlet should be changed. From studying the velocity vectors, no backflow is present. From this, it can be assumed that the number of guide vanes calculated in subsection 4.1.1 is adequate.
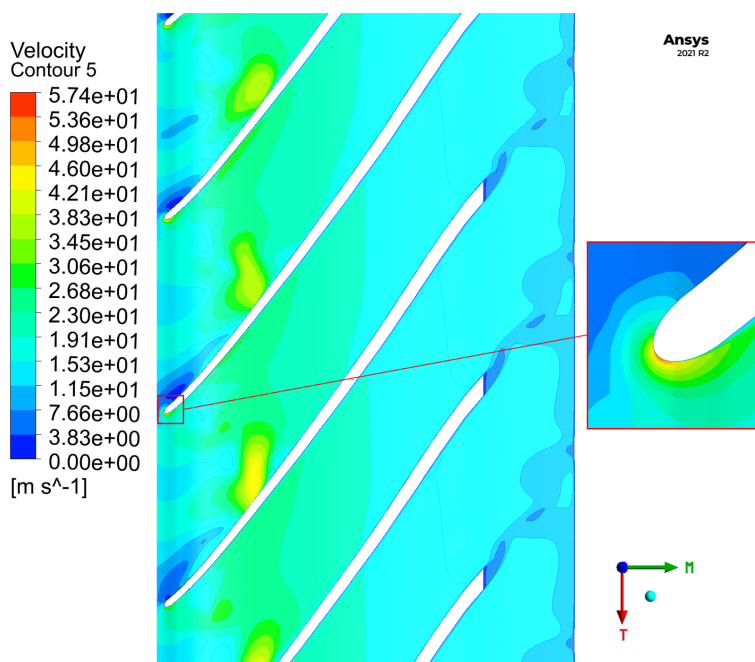
Figure 4.13: Velocity contours along the runner blades. The highest velocity occurs at the leading edge.

From looking at the velocity distribution along the blades in Figure 4.13 it is observed vortex shedding forming at the trailing edge, caused by the trailing edge shape. As explained in section 3.1, Ansys CFX captures vortex phenomena during steady-state simulations. The forming of vortex shedding should be further investigated, as it can cause problems such as vibrations and resonance.

4.3.4 Draft tube

From studying the velocity vectors at the draft tube inlet, an irrotational runner outlet is observed. In Figure 4.14 the velocity distribution at the draft tube inlet is given. As can be seen, the velocity is highest at the outlet diameters outside the boundary layer. The velocity is zero at the center due to the runner cone.

42
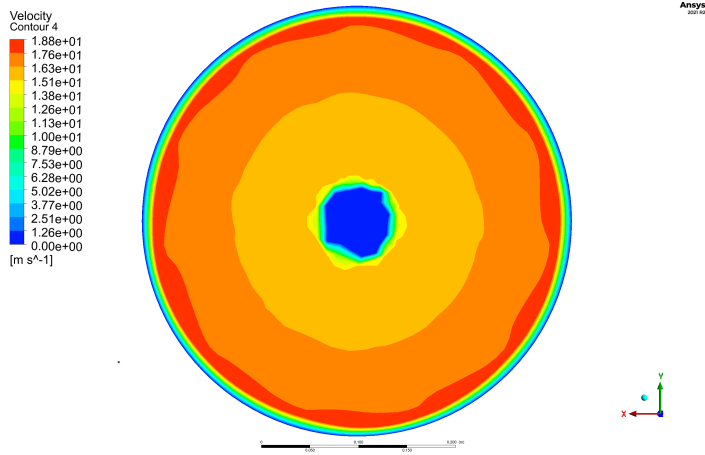
Figure 4.14: Velocity contour at the runner outlet.

4.4 Performance for different flow rates

To account for the decreased cooling demand and thereby flow over the years, simulations are run for different GVOs. All GVOs along with their corresponding flow rates, torque, and efficiency are displayed in Table 4.3. When discussing the performance of the turbine, it is necessary to look at the torque acting on the runner, not only the efficiency. This is due to the fact that all surfaces are assumed to be smooth.

As a reference, the state-of-the-art design obtains a torque of about 9000 Nm [3]. The base case gave a resulting efficiency of 83% and torque of 11000 Nm, which is reasonable as simulations in this project are done for a higher rotational speed.

Table 4.3: Results of the different guide vane openings simulated for different flow rates

Flow rate (m^3/s)	GVO (°)	M (Nm)	η (%)
$^*Q$	33.5	12000	0.83
$^*Q \cdot 0.5$	15.2	-2105	-0.30
$^*Q \cdot 0.75$	21.1	3334	0.32
$^*Q \cdot 0.75$	24.1	3117	0.30
$^*Q \cdot 0.75$	27.1	2915	0.28

A simulation was run for the minimum flow rate, $^*Q \cdot 0.5$, which resulted in a negative torque and efficiency. This indicates that the turbine operates in reverse pump mode, as described in Figure 3.1. Hence, an increased flow rate of $^*Q \cdot 0.75$ with a corresponding GVO of 24.1° was approached. It obtained an efficiency of 30% along with a positive torque. To identify the trend, two additional simulations were run for a lower and a higher GVO. Looking into the cause of the low efficiency, the simulations show that the guide vanes give the water an angle directing it straight to the runner's leading edge. Consequently, a lot of kinetic energy is wasted in the wake of the impact.

The resulting positive efficiency for each GVO is displayed in Figure 4.15. It can be observed that for $^*Q \cdot 0.75$ the efficiency increased with a decreased GVO, indicating that the best GVO for the specific flow rate is in fact below the calculated value of 24.1°. Due to limited time at this point, no further simulations were run to find the peak of the efficiency curve.
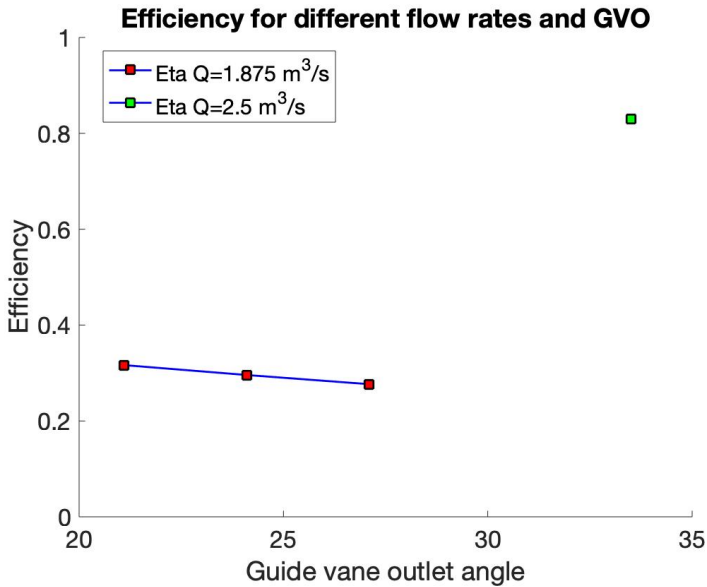

Figure 4.15: Efficiency curve for different GVOs.

———————————Chapter 5———————————

Conclusions

In this thesis, a numerical model of a complete Francis turbine is developed, including stay vanes, adjustable guide vanes, a runner, and a draft tube. The design is based on the principles of high head Francis theory, taking into account the limitations of the reference design and conducting CFD analysis. The efficiency of the turbine operated at different flow rates is also investigated. The efficiency showed a fair agreement with the efficiency achieved by Framo when operating their SWL pump as a turbine. This indicates that the computational model established gives realistic results, and is able to describe the problem accurately.

The analysis of the stay vanes reveals that the induced spin ceases before reaching the guide vanes. This issue is attributed to the gap between the stay vanes and the guide vane hub. Suggestions for improvement include reducing this gap to allow for a smoother transition and gradually curving the stay vanes upstream. Additionally, increasing the number of stay vanes may enhance the flow direction and acceleration.

Due to the ceased spin from the stay vanes, the water enters the guide vanes with an angle that induces flow separation on the suction side. The design of the guide vanes, particularly the leading edge, also contributes to reduced efficiency. The study recommends investigating the use of an asymmetric leading edge and reducing the number of guide vanes to achieve a more even distribution of the load and reduce friction losses.

The analysis of the runner indicates negative pressure on the suction side, particularly near the shroud and leading edge, while the pressure side experiences negative pressure at the trailing edge. The negative pressure may be attributed to the suboptimal inlet conditions caused by the stay vanes and the design of the leading edge. No backflow is observed, indicating that

the number of runner blades is sufficient. The velocity distribution along the runner blades shows vortex shedding at the trailing edge, which should be further investigated to avoid potential problems such as vibrations and resonance.

The draft tube analysis shows that the flow entering the draft tube is irrotational, indicating that all the kinetic energy is utilized in the runner.

To further investigate the turbine's performance, simulations were conducted at different flow rates by varying the guide vane openings (GVOs). At the minimum flow rate of $^*Q \cdot 0.5$, a negative torque and efficiency were observed, indicating that the turbine was operating in reverse pump mode. However, by increasing the flow rate to $^*Q \cdot 0.75$ and adjusting the GVO, positive efficiency and torque were achieved, although at a relatively low level. It is recommended to conduct a new efficiency study once the modifications described for the various turbine components have been implemented.

In conclusion, this thesis successfully establishes a numerical model of a complete Francis turbine, considering various components and design considerations. The analysis highlights areas for improvement in terms of component design, flow patterns, and efficiency. The findings contribute to the overall understanding of Francis turbine performance and provide insights for future optimization and design refinements.

—————————————————— Chapter 6——————————————————

Future work

To further enhance the performance of the turbine, several aspects can be explored in future investigations. One area with significant improvement potential is the stay vanes, where enhancing the spin of the unit can be achieved by increasing the number of stay vanes, adjusting the outlet angle, extending the length, and using the proposed stay vane outlet design. Once the stay vanes have been optimized, a simulation should be performed with the asymmetric guide vanes shown in Figure F.1. Considering that the current ratio between Z_{rb} and Z_{gv} is nearly doubled, it is worth considering reducing the value of Z_{gv}. This adjustment will reduce friction losses and achieve a more even distribution of the load. When the flow rate is reduced by 25%, there is a noticeable decrease in efficiency, even when the guide vane opening is decreased. Further efficiency studies should be conducted when the design improvements have been implemented.

Moving on to the runner blades, a lean angle study should be conducted. Pursuing the theory regarding lean angle from [12] and [13], the regulation of pressure balance within the runner can be enhanced. As Tiwari et. al [14] concluded, runner core cavitation is more likely to occur during part load operations. This should be a primary focus once the GVOs are optimized.

Other measures to consider include investigating the length of the guide vanes and the thickness of the runner blades, and conducting a detailed study of the leading and trailing edge shapes. Finally, it is crucial to ensure that all design modifications align with mechanical considerations, as the current thesis focuses solely on the fluid mechanical perspective.

References

[1] Gjøsæter, K., 2011, "Hydraulic Design of Francis Turbine Exposed to Sediment Erosion," Msc, Norwegian University of Science and Technology, Trondheim, Norway.

[2] Wei, Z., Finstad, P. H., Olimstad, G., Walseth, E., and Eltvik, M., 2009, "High Pressure Hydraulic Machinery," .

[3] 2023, "Framo wins OTC Spotlight Award," accessed 4.5.2023, https://www.framo.com/news/framo-wins-otc-spotlight-on-new-technology-award2/

[4] 2022, "Internasjonalt samarbeid for klimaet: Klimatoppmøter og Parisavtalen," accessed 3.5.2023, https://www.wwf.no/klima-og-energi/klimaforhandlinger

[5] 2022, "Emissions to air," accessed 3.5.2023, https://www.norskpetroleum.no/en/environment-and-technology/emissions-to-air/

[6] 2023, "Reducing CO2 Emissions From FPSOs," accessed 4.5.2023, https://www.maritimemagazines.com/offshore-engineer/202301/reducing-co2-emissions-from-fpsos/

[7] 2022, "Sustainability report 2021," accessed 4.5.2023, https://akerbp.com/wp-content/uploads/2022/03/aker-bp-sustainability-report-2021.pdf

[8] 2022, "Annual report 2021: Performance review and impact," accessed 4.5.2023, https://2021.annualreport.sbmoffshore.com/performance-review-impact/performance-review/emissions

[9] 2022, "Yinson's climate goal roadmap," accessed 4.5.2023, https://www.yinson.com/data/ckfinder/files/Yinson_s_Climate_Goals_Roadmap_WEB_22_10_2021_.pdf

[10] Tiwari, G., Kumar, J., Shukla, S., Prasad, V., and Patel, V., 2023, "Multi-Fidelity CFD Approach for Hydrodynamic Performance Analysis of a Prototype Francis Turbine- A Comparative Study," Fluid Mechanics and Fluid Power, **2**, pp. 123–128.

[11] Tiwari, G., Prasad, V., Shukla, S., and Patel, V., 2019, "Hydrodynamic analysis of a low head prototype Francis turbine for establishing an optimum operating regime using CFD," Journal of mechanical engineering and sciences, **14**(2), p. 6625–6641.

[12] Ayli, E., Celebioglu, K., and Aradag, S., 2016, "Determination and generalization of the effects of design parameters on Francisturbine runner performance," Engineering applications of computational fluid mechanics, **10**, pp. 545–564.

[13] Ma, Z., Zhu, B., Rao, C., and Shangguan, Y., 2019, "Comprehensive Hydraulic Improvement and Parametric Analysis of a Francis Turbine Runner," Energies, **12**, p. 307.

[14] Tiwari, G., Shukla, S. N., Prasad, V., and Patel, V. K., 2020, "Numerical investigation of hydrodynamics of the cavitating turbulent flow in a low head prototype francis turbine," AIP Conference Proceedings, **2273**(1).

[15] Sumer, B. and Fuhrman, D., 2020, Turbulence in Coastal and Civil Engineering, Advanced Series on Ocean Engineering, World Scientific, Singapore.

[16] ANSYS, 2021, "Ansys CFX-Solver Theory Guide," .

[17] Ferziger, J. H. and Perić, M., 2001, Computational Methods for Fluid Dynamics, Springer.

[18] Kundu, P., Cohen, I., and Rowling, D. R., 2015, Fluid Mechanics, Elsevier Science.

[19] Bernard, P. S., 1986, "Limitations of the near-wall k-ϵ turbulence model," AIAA, **24**, pp. 619–622.

[20] Menter, F. R., 1993, "Zonal Two Equation k-w Turbulence Models For Aerodynamic Flows," doi:10.2514/6.1993-2906.

[21] ANSYS, 2021, "Ansys TurboGrid User's Guide," .

[22] ANSYS, 2021, "Ansys Meshing User's Guide," .

[23] Trivedi, C., Personal conversation, 2023-01-16 to 2023-06-04.

[24] 2008, "Procedure for Estimation and Reporting of Uncertainty Due to Discretization in CFD Applications," Journal of Fluids Engineering, **130**(7).

[25] "3 Criteria for Assessing CFD Convergence," accessed des. 15, 2022, https://www.engineering.com/story/3-criteria-for-assessing-cfd-convergence

[26] 2021, "Examining Iterative Convergence," accessed 7.6.2023, https://www.grc.nasa.gov/www/wind/valid/tutorial/iterconv.html

[27] Brekke, H., 2003, "Pumper & Turbiner," Compendium.

[28] Kamran, M. and Fazal, M. R., 2021, "Chapter 6 - Hydro energy," Renewable Energy Conversion Systems, Academic Press, pp. 193–219.

[29] Halder, P., Doppalapudi, A. T., Azad, A. K., and Khan, M., 2021, "Chapter 7 - Efficient hydroenergy conversion technologies, challenges, and policy implication," Advances in Clean Energy Technologies, A. K. Azad, ed., Academic Press, pp. 295–318.

[30] Storli, P.-T., Personal conversation, 2023-01-09 to 2023-06-06.

[31] Lund, S., 2023, "Hydraulic design of a pump as a turbine for energy recovery purposes," M.Sc. thesis/project, Norwegian University of Science and Technology.

[32] Vangdal, N., Personal conversation, 2023-01-09 to 2023-05-15.

[33] Bitter, J. G. A., 1963, "A study of erosion phenomena part 1," Wear, **6**, pp. 5–21.

[34] Brekke, H., 1995, "Grunnkurs i Hydrauliske Strømningsmaskiner," Vannkraftlaboratoriet NTH.

[35] Brekke, H., 2015, "Hydraulic Turbines Design, Erection and Operation," , p. 317.

[36] Pierre, H., 1992, "Turbomachines hydrauliques," Presses polytechniques et universitaires Romand.

[37] Bergmann-Paulsen, J., 2012, "FSI-analysis of a Francis turbine," M.Sc. thesis/project, Institutt for energi- og prosessteknikk.

[38] Koirala, R., Thapa, B., Neopane, H. P., and Zhu, B., 2017, "A review on flow and sediment erosion in guide vanes of Francis turbines," Renewable and Sustainable Energy Reviews, **75**, pp. 1054–1065.

Appendix A – Reference design

A.1   State-of-the-art

Figure A.1 illustrates the performance diagram of the state-of-the-art design. It is important to note that this is based on a design without adjustable guide vanes.

A.2   Reference design

Figure A.2 illustrates a meridional view of the reference design. The runner is represented by the red domain, while the guide vanes and stay vanes are depicted by the shorter and longer green domains, respectively.

PERFORMANCE DIAGRAM FOR FRAMO TURBINE

Project no:	- -A			Rated point :	
Turbin type:	ST400/700-1	Medium:	Sea Water	Flow [m^3/hr]	6500
Number of stages	1	Density	1025 kg/m^3	Head [mlc]	60,0
Imp.drg.no:	2005-203-4	Visc:	1 cSt	Hydraulic Power [kW]	913
Imp.diam:	800 mm	Temp:	25 deg	Electric Power [kW]	840
Speed:	910 rpm	Dif. dgr. no:	2005-212-4	Hydraulic Efficiency [%]	84,4

		Sign	Date	-	1 x 70%
This document is the property of FRAMO AS. It is not to be reproduced or published without our written consent	Constr.	ACE	18.08.22	ST400/700-1	
	Checked	NV	19.08.22		
FRAMO an Alfa Laval brand				TAG:	

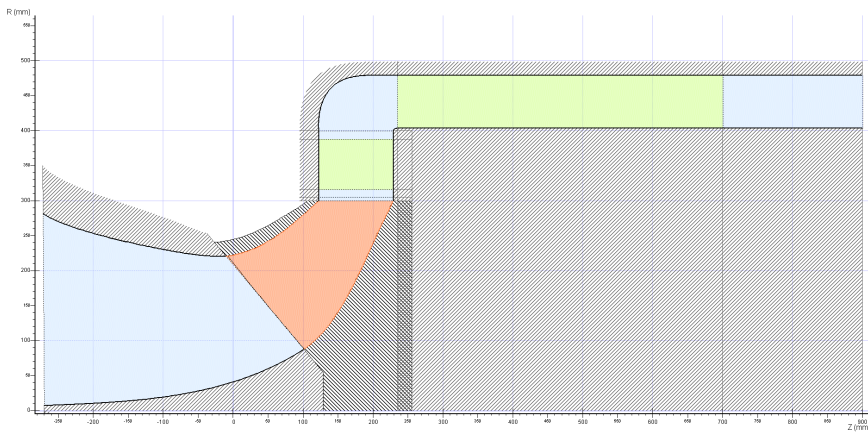**Figure A.1:** Performance diagram for Framo the reference design [3].

Figure A.2: Meridional view of the reference design, adapted by [3].

Reference design   Reference design   Reference design

—————————— Appendices ——————————

Appendix B – Matlab code

B.1   Main dimensions

```matlab
clear all; close all; clc

%% MAIN DIMENSIONS CALCULATION
% Made out from the equations stated in 3.2.1 Main dimensions
% Modified to fit the design in this case
% Mari Størksen

%% Given values
Q=2.5; %[m^3/s]
n=1010; %[rpm] med slip i guess
omega= 2*pi*n/60; %[m^2/s]
g=9.81; %[m/s^2]
H=60; %[m]
eta_h=0.96; %hydraulic efficiency

D2=0.47; %[m]
D1=0.54; %[m]
K_accel=1.1; %acceration of cm through runner


%% Outlet calculations:
red=sqrt(2*g*H); %reference velocity c (red since it is used
↪    to find reduced variables)

cu2=0; %no swirl at BEP
```

```matlab
u2_red=D2/2*omega/red; %reduced peripheral outlet velocity
u2=u2_red*red; %peripheral outlet velocity

cm2=4*Q/(pi*D2^2); %absolute outlet velocity
c2=cm2; %meridional outlet velocity.

beta_2=atan(cm2/u2); %outlet angle in radians
beta_2_deg=beta_2*180/pi; %outlet angle in degrees

w2=sqrt(u2^2+c2^2); %outlet relative velocity


%% Inlet calculations

u1_red=D1/(2*red/omega); %reduced peripheral inlet velocity
cu1_red=eta_h/(2*u1_red); %reduced peripheral component of
↪   abs. velocity

u1=u1_red*red; %peripheral inlet velocity
cu1=cu1_red*red; %peripheral component of abs. velocity

cm1=cm2/K_accel; %meridional inlet velocity
B1=Q/(pi*D1*cm1); % the maximum height is 0.132 from the
↪   volute.
beta_1=atan(cm1/(u1-cu1)); %inlet angle in radians
beta_1_deg=beta_1*180/pi; %inlet angle in  degrees
alfa1=rad2deg(atan(cm1/cu1));

c1=cm1/sin(deg2rad(alfa1)); %absolute inlet velocity
w1=cm1/sin(beta_1); %relative inlet velocity

angle_sum=beta_1_deg+alfa1;
```

B.2   Number of blades

```matlab
clear all; close all; clc

Q_ref=2.5;  %Flow given by Framo
```

```matlab
Wstart=28;      %Initial guess of relative velocity at suction
↪   side
D1=0.54;        %Inlet diameter
B=0.1125;       %Inlet height
r=D1;
Z=11;           %Number of blades
t=0.05;         %Blade thickness
n=pi*D1/Z-t;    %distance between two blades in a channel
steg=20;        %Number of steps
dn=n/(steg-1);       %step length

omega=105.7670; %found from main_dimension_design.m
beta1=0.9811;   %found from main_dimension_design.m
wintern=1;
W(1)=Wstart;    %Initial value
Cm(1)=W(1)*sin(beta1);  %initial value
Q=0;

for i=2:steg
    dW=(-2*omega-W(i-1)/r)*dn;
    W(i)=W(i-1)+dW;
    Cm(i)=W(i)*sin(beta1);
    Q_B=Cm(i)*dn*B;

    Q =Q + Q_B;
    wintern=W(i);
end
Q = Q*Z;

if Q > Q_ref
    fprintf('backflow appears, increase number of blades')
else
    fprintf('No backflow')
end
```

B.3   Blade geometry

B.3.1   main dimension design.m

```matlab
clear all; close all; clc
%% Main dimensions of a high pressure Francis turbine
g=9.8; rad=pi/180; %constant

% Input and Choices
Hn=60; Qn=2.5;
a=1.1; b=0.1; beta2=30.1028*rad; U2=24.8552;
enta_hydraulic=0.96; u_1=0.8323; Cu2=0; % u_1 is u1 reduced

% calculate the reduced constant
red=sqrt(2*g*Hn);

%% calculate the main dimension of runner
Cm2=U2*tan(beta2);


Nn=1010;
D2=0.47;
u1=u_1*red;
D1=0.54;
u2=pi*Nn*D2/60;
cm2=Qn*4/pi/D2^2;
accel=1.1;
cm1=cm2/accel;
B1=accel*D2^2/4/D1;
cm_1=cm1/red;
cu_1=enta_hydraulic/(2*u_1);
cu1=cu_1*red;
beta1=atan(cm_1/(u_1-cu_1));
w1=cm1/sin(beta1);
omega=2*pi*Nn/60;
alpha1=atan(cm1/cu1);


NPSH=(a*cm2^2-b*u2^2)/2/g;
Nrbnumber=11; % the number of runner blades

speednumber=pi*Nn/30/red*sqrt(Qn/red) ;
```

```matlab
%% Guide vanes dimension
Dgvo=1.05*D1;
Bgv=B1;
cugvo=cu1*D1/Dgvo;
cmgvo=Qn/(pi*Bgv*Dgvo);
alphagvo=atan(cmgvo/cugvo);
Ngv=16; % choose
Daxf=D1*(0.29*speednumber+1.07);% first guess
Lgv=pi*Daxf/2/Ngv;
Dgvi=2*sqrt(Lgv^2+(Dgvo/2)^2-Lgv*Dgvo*cos(pi/2+alphagvo));
alphagvi=pi/2-acos((Lgv^2+Dgvi^2-Dgvo^2)/(2*Lgv*Dgvi));
cmgvi=Qn/(Dgvi*Bgv*pi);
cugvi=cmgvi/tan(alphagvi); %Til hit er det brukt Tokke power
↪   plant-kode
Dgv0=2*sqrt((Lgv*2/3)^2+(Dgvo/2)^2-
↪   Lgv*2/3*Dgvo*cos(pi/2+alphagvo)); %hentet fra Design of a
↪   reversible pump turbine
alphagv0=pi/2-acos( ( Dgv0^2 + Lgv^2-Dgvo^2)/ (2*Dgv0*Lgv));


% Regner ut gv-punkter for NACA0016 fra Tokke
tgv=Lgv*0.30;
itr=1000; %valgt for høy nøyaktivhet i plottingen av gv
xgv=0:Lgv/itr:Lgv;
xgv=xgv';
ygv=tgv*Lgv/.2*(.2969*(xgv/Lgv).^.5-.1260*(xgv/Lgv)-
↪   .3516*(xgv/Lgv).^2+.2843*(xgv/Lgv).^3-.1015*(xgv/Lgv).^4);
↪


% %%
%
% % Egenkomponert
% %Samle x og y til en felles matrise for punktene oppe og
↪   nede
% gv_points=zeros(2002,2);
% for j=1:1000
%          gv_points(j,1)=xgv(j,1);%*10^3;
%          gv_points(j,2)=ygv(j,1);%*10^3;
% end
```

61

```
% n=1000;
% for i=2002:-1:1002 %102:202
%     n=n+1;
%         gv_points(n,1)=xgv(i-1001,1);%*10^3;
%         gv_points(n,2)=-ygv(i-1001,1);%*10^3;
% end
%
%
% %Rotere gv til riktig vinkel
% R = @(theta) [cos(theta), -sin(theta); sin(theta),
↪   cos(theta)]; %takk til Johannes Djupesland for hjelp
% gv_rotated = R(alphagv0+pi)*gv_points';
%
% figure(32); clf; %hold on
% plot(gv_rotated(1,:),gv_rotated(2,:),'Linewidth',1);
%
% %Flytte gv til riktig radius
% gv_moved=zeros(3,2002);
% for i=1:2002
%     gv_moved(1,i)=gv_rotated(1,i)+Lgv*cos(alphagv0);%+Dgvi;
%
↪   gv_moved(2,i)=gv_rotated(2,i)+Dgvo/2+Lgv*sin(alphagv0);%*10^3;
% end
%
% %Spaceclaim er innstilt på mm så gjør om til det her;
% gv_cfx=gv_moved';%*10^3;
%
% %Plotting av gv etter den er flyttet
% figure(33); clf; %hold on
% plot(gv_moved(1,:),gv_moved(2,:),'Linewidth',1);
% legend('NACA 0016','Fontsize',17);
% title('Guide vane with NACA 0016 profile');
% xlabel('X','Fontsize',12); ylabel('Y','Fontsize',12);
% %axis=([0 0.045 0.2 0.235],'Fontsize',12);
% set(gca,'FontSize',17)
% axis equal

%% Ny guide vane
%a=90-63.9;
%b=33.5+90;
%c=180-b-a;
```

62

```matlab
%Lgv1=sin((c)*pi/180)/sin((b)*pi/180)*0.375;
Lgv=0.13;
n = 10; %steg
alphagvi_sh = 53*pi/180;
alphagvi_hu = 63.9*pi/180;

%Shroud
d_alpha_sh = alphagvi_sh - alphagvo;
da_sh = d_alpha_sh/n;
%Hub
d_alpha_hu = alphagvi_hu - alphagvo;
da_hu = d_alpha_hu/n;
%Gjennomsnitt
d_alpha_avg=(alphagvi_hu+alphagvi_sh)/2-alphagvo;

dr=Lgv/(n-1);

gv_init_sh = zeros(2,10);
gv_init_sh(1,1)=0;
gv_init_sh(2,1)=0;%0.2835;

gv_init_hu=gv_init_sh;

for i = 2:10
    gv_init_sh(1,i) = gv_init_sh(1,i-1) + dr*cos(da_sh);
    gv_init_sh(2,i) = gv_init_sh(2,i-1) + dr*sin(da_sh);

    gv_init_hu(1,i) = gv_init_hu(1,i-1) + dr*cos(da_hu);
    gv_init_hu(2,i) = gv_init_hu(2,i-1) + dr*sin(da_hu);
end
figure(59)
plot(gv_init_sh(1,:),gv_init_sh(2,:))
hold on
plot(gv_init_hu(1,:),gv_init_hu(2,:))
legend('shroud','hub')
axis equal

tgv=Lgv*0.30;
itr=1000; %valgt for høy nøyaktivhet i plottingen av gv
xgv=0:Lgv/itr:Lgv;
xgv=xgv';
```

```matlab
ygv=tgv*Lgv/.2*(.2969*(xgv/Lgv).^.5-.1260*(xgv/Lgv)-
↪    .3516*(xgv/Lgv).^2+.2843*(xgv/Lgv).^3-.1015*(xgv/Lgv).^4);
↪

gv_points=zeros(2002,2);
for j=1:1000
        gv_points(j,1)=xgv(j,1);%*10^3;
        gv_points(j,2)=ygv(j,1);%*10^3;
end
n=1000;
for i=2002:-1:1002 %102:202
    n=n+1;
        gv_points(n,1)=xgv(i-1001,1);%*10^3;
        gv_points(n,2)=-ygv(i-1001,1);%*10^3;
end


%Rotere gv til riktig vinkel
R = @(theta) [cos(theta), -sin(theta); sin(theta),
↪    cos(theta)]; %takk til Johannes Djupesland for hjelp
gv_rotated = R(d_alpha_avg+pi)*gv_points';%d_alpha_sh+pi

figure(32); clf; %hold on
plot(gv_rotated(1,:),gv_rotated(2,:),'Linewidth',1);
axis equal
%Flytte gv til riktig radius
gv_moved=zeros(3,2002);
for i=1:2002

↪    gv_moved(1,i)=gv_rotated(1,i)+Lgv*sin(d_alpha_avg);%gv_rotated(1,i)+Lgv*cos

↪    gv_moved(2,i)=gv_rotated(2,i)+Dgvo/2;%+Lgv*sin(d_alpha_hu);%gv_rotated(2,i)
end

%Spaceclaim er innstilt på mm så gjør om til det her;
gv_cfx=gv_moved'*10^3;

%Plotting av gv etter den er flyttet
figure(33); clf; %hold on
plot(gv_moved(1,:),gv_moved(2,:),'Linewidth',1);
legend('NACA 0016','Fontsize',17);
title('Guide vane with NACA 0016 profile');
```

```matlab
xlabel('X','Fontsize',12); ylabel('Y','Fontsize',12);
%axis=([0 0.045 0.2 0.235],'Fontsize',12);
set(gca,'FontSize',17)
axis equal
```

B.3.2   kjordenne.m

```matlab
clear all; close all; clc
main_dimension_design
%input D1,D2,B1
D1=0.54;
D2=0.47;
B1=0.1125;
Q=Qn;
% Nn=375
% Nrbnumber=13
beta1=0.9811 ;
beta2=0.5254;

Np=15; % Number of points along the streamline
Ns=5; %Number of stremlines
R1=D1/2; %Inlet
R2=D2/2; %Outlet
a=0.07;
b=0.45*D2; % Assumption
c=R1-R2;
z_null=0.5;
ellipse=[a,b]; %a, b in the ellipsis equation
integral=0;
step_integral=100000; %%%% *** very important, it should be as
↪  big as possible,then you can get the accurate value ^_^
integral_start=-c; %Start of integral
integral_end=0; %End of intergral
dx=(integral_end-integral_start)/step_integral;

% First integration to find the length of the line. (bottom
↪  line)
for x=integral_start:dx:integral_end
```

```matlab
    dydx=0.5*b*((1-(x/a)^2)^(-0.5))*(-2*x/a^2); % dydx denotes
↪   dy/dx, it means the slope of curve.
integral=integral+(((1+(dydx)^2)^0.5)*dx); % this is the
↪   equation to calculate the length of arc.
end
%Defining the matrix for the coordinates
X=zeros(Np, Ns);
Y=zeros(Np, Ns);
R=zeros(Np, Ns);
Z=zeros(Np, Ns);
alpha=zeros(Np, Ns);
length=integral;
ds=length/(Np-1);
i=Np+1;
% j=1


%Dividing the line into equal sections
%moving the arc
for s = 0:ds:length
i = i-1;
integral = 0;
x = -c;
while integral < s
    x=x + dx;
    dydx=0.5*b*((1-(x/a)^2)^(-0.5))*(-2*x/a^2);
    integral=integral+(((1+(dydx)^2)^0.5)*dx);
end

X(i,1)=x+c+R2 ;
Y(i,1)=sqrt((b^2)-((b*x/a)^2))+z_null;
R(i,1)=X(i,1);
Z(i,1)=Y(i,1);
end

%Starts calculating the known points: R(1,j) and Z(1,j)
delta_b=B1/(Ns-1);

for j=1:Ns-1
    Z(1,j+1)=Z(1,j)+delta_b;
    R(1,j+1)=R(1,1);
end
```

```matlab
% calculate alpha(:,1)
alpha(2:Np-1,1)=atan((Z(1:Np-2,1)-Z(3:Np,1))./(R(1:Np-2,1)-
↪   R(3:Np,1)));
↪
alpha(Np,1)=atan((Z(Np-1,1)-Z(Np,1))./(R(Np-1,1)-R(Np,1)));

%calculating the values for the area

A=zeros(Np,1);
A(1)=B1/(Ns-1)*pi*D1;
for k=2:Np
    A(k)=A(1)/(1+0.1*k/Np);
end

% j=1
% i=2
for j=2:1:Ns
R(2:Np,j) =
↪   (R(2:Np,j-1).^2-A(2:Np).*sin(alpha(2:Np,j-1))/pi).^0.5;
Z(1:Np,j) = Z(1:Np,j-1)+A(1:Np).*cos(alpha(1:Np,j-
↪   1))./(pi*(R(1:Np,j)+R(1:Np,j-1)));
alpha(2:Np-1,j)=atan((Z(1:Np-2,j)-Z(3:Np,j))./(R(1:Np-2,j)-
↪   R(3:Np,j)));
alpha(Np,j) = atan((Z(Np-1,j)-Z(Np,j))./(R(Np-1,j)-R(Np,j)));
end

figure(1)
clf;
plot(R, Z, '-bs',...
    'LineWidth',1,...
    'MarkerEdgeColor','k',...
    'MarkerFaceColor','g',...
    'MarkerSize',4)
 xlabel('Radius,R'); ylabel('Height, Z'); title ('Axial view')


%define energy distribution
cm2=Q*4/pi/D2^2;
cm1=cm2/1.1;
deltacm=(cm2-cm1)/(Np-1);
%u_1=0.725;
```

```matlab
reducedconst=sqrt(2*g*Hn);
u1=u_1*reducedconst;
cu1=u1-cm1/tan(beta1);
ucu1=u1*cu1;
w1=sqrt((u1-cu1)^2+cm1^2);
ucupoint=[0,0.0625,0.375,0.5625,0.6875,0.8125,0.875]; %S1 is
↪    the bottom
%stream line
UCurelativedist=[1,0.78,0.25,0.1,0.05,0.02,0];
% UCurelativedist=UCu/UCumax;


p=polyfit(ucupoint,UCurelativedist,6); p1=p(1);
p2=p(2);
p3=p(3);
p4=p(4);
p5=p(5);
p6=p(6);
p7=p(7);
% %y=6.4248*x^6+x^5*(-25.4288)+x^4*(37.5163)-
↪    x^3*27.4488+x^2*12.0268-
↪    x*4.1732+1


integral=0;
step_integral=100000; % very important, it should be as big as
↪    possible,then you can get the accurate value ^_^
integral_start=0;
integral_end=0.875; % End of intergral
dx=(integral_end-integral_start)/step_integral;
%
for x = integral_start:dx:integral_end
dydx=6.4248*x^5*6+x^4*(-25.4288)*5+x^3*(37.5163)*4-
↪    x^2*27.4488*3+x*12.0268*2-4.1732;
integral=integral+(((1+(dydx)^2)^0.5)*dx);
end

% Defining the matrix for the coordinates
S1=zeros(Np, 1); % S1 denotes the bottom streamline
UCurelativedist=zeros(Np, 1);
length=integral;
ds=length/(Np-1);
i=Np+1;
```

```matlab
% Dividing the line into equal sections
for s = 0:ds:length
    i = i-1;
    integral = 0;
    x =0;
    while integral < s
        x=x + dx;
        dydx=6.4248*x^5*6+x^4*(-25.4288)*5+x^3*(37.5163)*4-
x^2*27.4488*3+x*12.0268*2-4.1732;
        integral=integral+(((1+(dydx)^2)^0.5)*dx);
    end
    S1(i)=x;
    UCurelativedist(i)=6.4248*x^6+x^5*(-
25.4288)+x^4*(37.5163)-
x^3*27.4488+x^2*12.0268-x*4.1732+1;
end

figure(100);
clf;
plot(S1,UCurelativedist, '-bs',...
    'LineWidth',1,...
    'MarkerEdgeColor','k',...
    'MarkerFaceColor','b',...
    'MarkerSize',4)
 xlabel('ucupoint');
 ylabel('UCu relative value');
 title ('Given the energy distribution along the ring')
% axis([0 1 0 1]);
for j=1:Ns
    for i=1:Np
    u(i,j)=(pi*Nn/30)*R(i,j);
    cm(i,j)=cm1+(i-1)*deltacm;
    ucu(i,j)=UCurelativedist(Np-i+1)*ucu1;
    cu(i,j)=ucu(i)/u(i,j);
    beta(i,j)=atan(cm(i,j)/(u(i,j)-cu(i,j)));
    w(i,j)=sqrt((u(i,j)-cu(i,j))^2+cm(i,j)^2);

    ucurelative(i,j)=ucu(i,j)/ucu1;
    urelative(i,j)=u(i,j)/u1;
    curelative(i,j)=cu(i,j)/cu1;
```

69

```matlab
        cmrelative(i,j)=cm(i,j)/cm1;
        wrelative(i,j)=w(i,j)/w1;
        betarelative(i,j)=beta(i,j)/beta1;
        end
end


% calculate G-H-plane!!!
G=zeros(Np,Ns);
dG=zeros(Np-1,Ns);
dH=zeros(Np-1,Ns);
d_theta=zeros(Np-1,Ns);
theta=zeros(Np-1,Ns);


%G
for j=1:1:Ns
dG(1:end,j) = ((R(1:end-1,j)-R(2:end,j)).^2+(Z(1:end-1,j)-
↪   Z(2:end,j)).^2).^0.5;
G(2:end,j) = G(1:end-1,j)+((R(1:end-1,j)-
↪   R(2:end,j)).^2+(Z(1:end-1,j)-Z(2:end,j)).^2).^0.5;
end


% H
for j=1:Ns
beta=beta(1:end,1);
dH(1:end,j)=dG(1:end,j)./tan(-beta(2:end,1)); %endre for andre
↪   retning
d_theta=2*dH./(R(1:end-1,:)+R(2:end,:));
end

Xr=zeros(Np-1, Ns);
Yr=zeros(Np-1, Ns);
for i=2:1:Np
    theta(i,:)=theta(i-1,:)+d_theta(i-1,:);
end

Xr=R.*cos(theta); Yr=R.*sin(-theta); Zr=Z; %endre for andre
↪   retning


figure(2)
clf;
```

```matlab
surf(Xr(1:end,:),Yr(1:end,:), Zr(1:end,:))
xlabel('X'); zlabel('Z'); ylabel('Y'); title ('3D blades')
figure (7); clf; hold on; axis equal
deltatheta=linspace(0,2*pi,Nrbnumber); % generates a row
↪    vector deltatheta of Nrbnumber points linearly spaced
↪    between and including 0 and 2*pi.

for dth=deltatheta
[Xr,Yr]=pol2cart(theta+dth,R); % Transform polar or
↪    cylindrical coordinates to Cartesian
h=surf(Xr(1:end,:),Yr(1:end,:), Zr(1:end,:));
end

figure(8); clf; hold on; grid on;
plot(Xr,Yr, '-bs',...
    'LineWidth',1,...
    'MarkerEdgeColor','k',...
    'MarkerFaceColor','g',...
    'MarkerSize',4)
xlabel('Radial direction - H'); ylabel('Axial direction -
↪    G');title ('G-H Plane')

%%% calculte the thickness of runner
P=1000*g*Hn*Q*0.96;%1.1*10^8; % the power of turbine
b1=B1;
a1=R(1,1)-R(floor(Np/2),1);
Rm=(R(floor(Np/2),1)+R(1,1))/2;
omega=Nn*pi/30;
sigma=10^8;
Delta_p=P/(Nrbnumber*a1*b1*omega*Rm);
trb=sqrt(2*(b1^2)*Delta_p/sigma);
% trb=0.0518;


theta_deg=theta*180/pi;
```

B.3.3   Energydistribution wei.m

```matlab
% energy distribution
%clear all; close all; clc
```

```matlab
kjordenne
mediumstream=floor(Ns/2); % mediumstream means the medium
↪   stream line
bottomstream=1;% ringstream means the lower stream line or the
↪   ring
upperstream=Ns;

betaTemp=zeros(Np,1);
betaTemp(1,1)=beta1;
betaTemp(2:end)=beta(2:end,1);

p=zeros(Np,1);
for i=1:1:Np
    p(i)=i;
end

figure(10);clf;hold on;grid on; axis([1 Np 0 3])
title('Energy and velocity distribution on the middle
↪   streamline');
xlabel('Section Number');
ylabel(' Values relative to the inlet values');
plot(p,ucurelative(:,mediumstream),'-k','Linewidth',1.3)
plot(p,curelative(:,mediumstream),'-r','Linewidth',1.3)
plot(p,urelative(:,mediumstream),'-g','Linewidth',1.3)
plot(p,cmrelative(:,mediumstream),'-b','Linewidth',1.3)
plot(p,wrelative(:,mediumstream),'-m','Linewidth',1.3)
plot(p,betarelative(:,mediumstream),'-co','Linewidth',1.3)
legend('ucu','cu','u','cm','w','beta','Location','northeast')
set(gca,'FontSize',17)

figure(11);clf;hold on;grid on; axis([1 Np 0 3])
title('Energy and velocity distribution on the shroud ');
xlabel('Section Number');
ylabel('Values relative to the inlet values');
plot(p,ucurelative(:,bottomstream),'-k','Linewidth',1.3)
plot(p,curelative(:,bottomstream),'-r','Linewidth',1.3)
plot(p,urelative(:,bottomstream),'-g','Linewidth',1.3)
plot(p,cmrelative(:,bottomstream),'-b','Linewidth',1.3)
plot(p,wrelative(:,bottomstream),'-m','Linewidth',1.3)
plot(p,betarelative(:,bottomstream),'-co','Linewidth',1.3)
legend('ucu','cu','u','cm','w','beta','Location','northeast')
```

```matlab
set(gca,'FontSize',17)

figure(13);clf;hold on; grid on; axis([1 Np 0 3])
title('Energy and velocity distribution on the hub ');
xlabel('Section Number');ylabel('Values relative to the inlet
↪   values');
plot(p,ucurelative(:,upperstream),'-k','Linewidth',1.3)
plot(p,curelative(:,upperstream),'-r','Linewidth',1.3)
plot(p,urelative(:,upperstream),'-g','Linewidth',1.3)
plot(p,cmrelative(:,upperstream),'-b','Linewidth',1.3)
plot(p,wrelative(:,upperstream),'-m','Linewidth',1.3)
plot(p,betarelative(:,upperstream),'-co','Linewidth',1.3)
legend('ucu','cu','u','cm','w','beta','Location','northeast')
set(gca,'FontSize',17)
```

B.4   Plots

```matlab
figure(1); clf; hold on; axis([20 35 0 1]);
plot([21.1 24.1 27.1],[0.316481 0.295844 0.276689],'-bs',...
    'LineWidth',1.4,...
    'MarkerEdgeColor','k',...
    'MarkerFaceColor','r',...
    'MarkerSize',8)
plot(33.5,0.830549,'-bs',...
    'LineWidth',1.4,...
    'MarkerEdgeColor','k',...
    'MarkerFaceColor','g',...
    'MarkerSize',8)
legend('Eta Q=1.875 m^3/s','Eta Q=2.5 m^3/s','Location', 'best');
ylabel('Efficiency','Fontsize',12);
xlabel('Guide vane outlet angle','Fontsize',12);
title('Efficiency for different flow rates and GVO');
%axis([1183777 2055484 69.38 69.56]);
set(gca,'FontSize',17)
%xlabel('X','Fontsize',12); ylabel('Y','Fontsize',12);

%set(gca,'FontSize',17)
```

```matlab
figure(1); clf;
plot([1183777 1710416 2054392 2352896],[373745 389864 402087
↪    402257],'-bs',...
    'LineWidth',1.4,...
    'MarkerEdgeColor','k',...
    'MarkerFaceColor','r',...
    'MarkerSize',8)
legend('Pressure at runner outlet','Location', 'best');
ylabel('Pressure [Pa]','Fontsize',12);
xlabel('Total number of elements','Fontsize',12);
title('Grid independence study');
%axis([1183777 2055484 69.38 69.56]);
set(gca,'FontSize',17)
%xlabel('X','Fontsize',12); ylabel('Y','Fontsize',12);
%axis=([0 0.045 0.2 0.235],'Fontsize',12);
%set(gca,'FontSize',17)
```

Appendix C – Main dimensions

Figure C.1 illustrates the parametric study conducted to find the most optimal D_1, D_2 and K_{accel}. The yellow row represents the chosen values and their corresponding angles and peripheral velocities. The choice is based on getting values close to the empirical values stated in subsection 3.2.1 and getting an angle between c_1 and w_1 close to $90°$.

D_1	D_2	K_accel	α_1	β_1	α_1+β_1	β_2	u_1	u_2	B_1
0,54	0,4	1,1	42,43	64,13	106,56	43,24	28,56	21,15	0,0815
0,54	0,35	1,1	50,05	69,63	119,68	54,54	28,56	18,51	0,0624
0,54	0,45	1,1	42,43	64,13	106,56	43,24	28,56	21,15	0,0815
0,54	0,5	1,1	30,33	52,85	83,18	25,71	28,56	26,44	0,1273
0,54	0,48	1,1	32,41	55,07	87,48	28,56	28,56	25,38	0,1173
0,54	0,47	1,1	33,51	56,2	89,71	30,1	28,86	24,86	0,1125
0,54	0,46	1,1	34,65	57,33	91,98	31,73	28,56	24,33	0,1078
0,54	0,47	1,2	31,25	53,86	85,11	30,1	28,86	24,86	0,1227
0,54	0,45	1,2	33,51	56,2	89,71	33,45	28,56	23,78	0,1125

Figure C.1: Parametric study done to determine the main dimensions.

Main dimensions   Main dimensions   Main dimensions

Appendices

Appendix D – GCI theory

The following theory concern the well-established approach Grid Convergence Index (GCI) as a lot of time was invested in it. All theory is adapted from Thapa et. al [24]. It origins from the theory of the generalized Richardson extrapolation method. It seeks to relate each refinement by determining "the apparent order of the solution convergence and the relative convergence error" for the flow performance.

The GCI procedure starts from defining a representative cell size, h_i, for each grid refinement, i, as Equation (D.1) demonstrates. Here, $h_1 < h_2 < h_3$. From empiricism, it is desirable that the corresponding grid refinement factor, $r = h_{coarse}/h_{fine}$, is above 1.3. It is preferable that the cells are geometrically similar, but not necessary.

Since each component behaves differently each grid size will have a strong influence on the total error. It is therefore crucial to perform an independent mesh study, meaning that the GCI is based on all components combined. Due to the difference in geometry, the grid size will not be constant. It is convenient to relate the average/max/min element size to the volume of the respective component. By ensuring that the ratio is equal for all components.

Turbogrid has the option to either remain the boundary layer constant for each grid refinement or refine it meaning the y^+ value will change as well. The former alternative will keep the blade loading constant, while the latter will make sure that the turbulence models are behaving differently according to the refinement. Neither of the consequences is preferable, but the constant boundary layer is chosen.

$$h_i = \left[\frac{1}{N} \sum_{i=1}^{N} (\Delta V_i) \right]^{1/3} \tag{D.1}$$

The apparent order of the method, p, is governed by Equation D.2.

$$p = \frac{1}{ln(r_{21})} \left| ln \left| \frac{\epsilon_{32}}{\epsilon_{21}} \right| + q(p) \right| \tag{D.2}$$

$\epsilon_{32} = \phi_3 - \phi_2$ and $\epsilon_{21} = \phi_2 - \phi_1$, where ϕ_i is a relative parameter found from the ith simulation, describing efficiency, drag or temperature depending of the case. If the ratio between ϵ_{32} and ϵ_{21} is negative, the convergence is oscillatory. It should be emphasized that if r is held constant then q(p) is equal to zero. This is not the case in this project, thus Equation (D.3) and (D.4) is used.

$$q(p) = ln \left(\frac{r_{21}^p - s}{r_{32}^p - s} \right) \tag{D.3}$$

$$s = sgn(\epsilon_{32}/\epsilon_{21}) \tag{D.4}$$

The extrapolated values can then be calculated as shown in Equation D.5. The following equations are calculated likewise for subscript 32.

$$\phi_{ext}^{21} = \frac{r_{21}^p \phi_1 - \phi_2}{r_{21}^p - 1} \tag{D.5}$$

Then, the approximate relative error, an updated extrapolated relative error, and the fine-grid convergence index can be calculated as Equation (D.6), (D.7) and (D.8), respectively.

$$e_a^{21} = \left| \frac{\phi_1 - \phi_2}{\phi_1} \right| \tag{D.6}$$

$$e_{ext}^{21} = \left| \frac{\phi_{ext}^{21} - \phi_1}{\phi_{ext}^{21}} \right| \tag{D.7}$$

Lastly, the grid convergence index is calculated. A GCI less than 1% is accepted as a converged solution.

GCI   GCI   GCI

$$GCI_{fine}^{21} = \frac{1.25 e_a^{21}}{r_{21}^p - 1} \tag{D.8}$$

GCI   GCI   GCI

Appendix E – Blade geometry plots

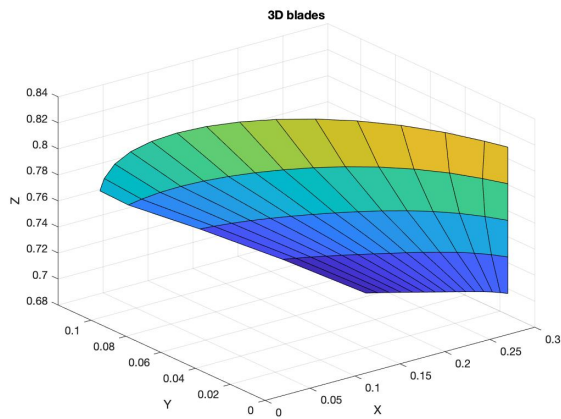The plots produced by the code in section B.3 that did not fit into the results is presented here.

Figure E.1: 3D view of the blade, without thickness.
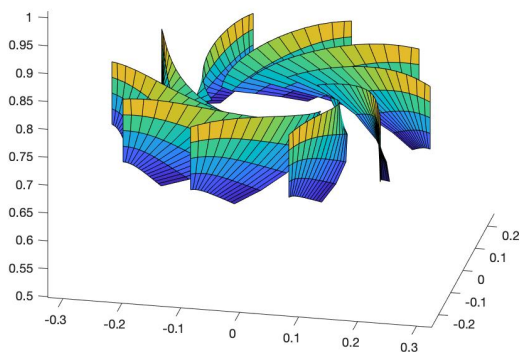
Figure E.2: 3D view of the runner, without blade thickness.
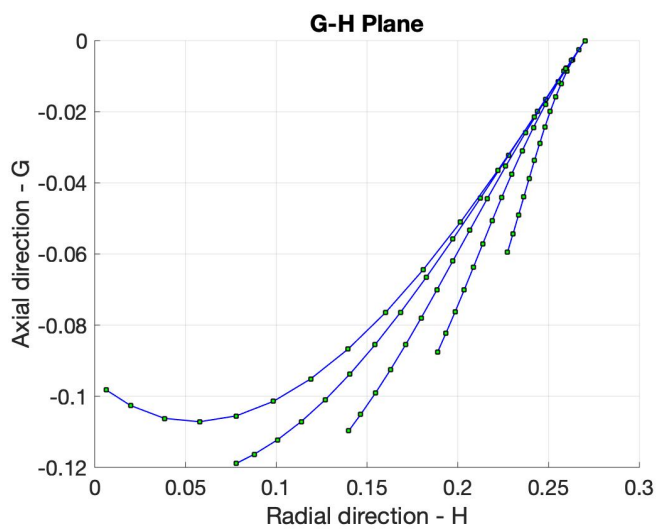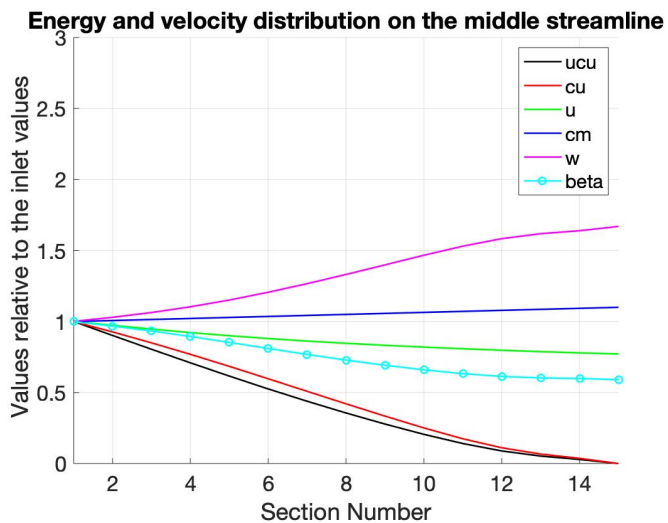

Figure E.3: G-H plot.

Figure E.4: Normalized energy distribution for the middle streamline.
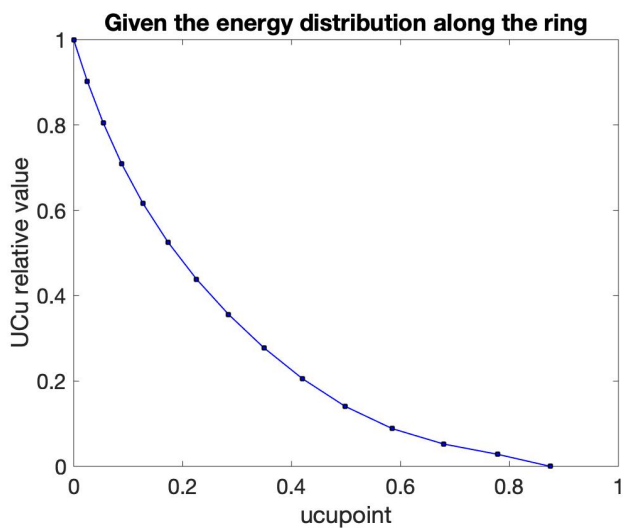

Figure E.5: Chosen $u \cdot c_u$ distribution.

Blade geometry plots   Blade geometry plots   Blade geometry plots

Appendix F – Initial guide vane design

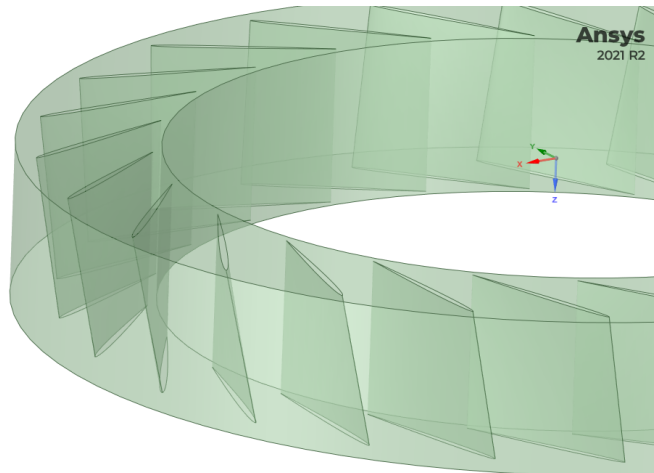The asymmetric guide vanes design is presented in Figure F.1.

Figure F.1: Asymmetric guide vane design. The gravity field is in the z-direction.

Guide vane design   Guide vane design   Guide vane design

Appendix F – Verification of the computational model

G.1 Number of elements

Table G.1: Number of elements for the different components and the unit as a whole

	Stay vanes	Guide vanes	Runner	Draft tube	Total
GCI_1	201852	104670	814678	62577	1183777
GCI_2	290880	145960	1184722	88854	1710416
GCI_3	348500	176988	1410448	118456	2054392
GCI_4	379400	206195	1648845	118456	2352896

G.2 Residuals

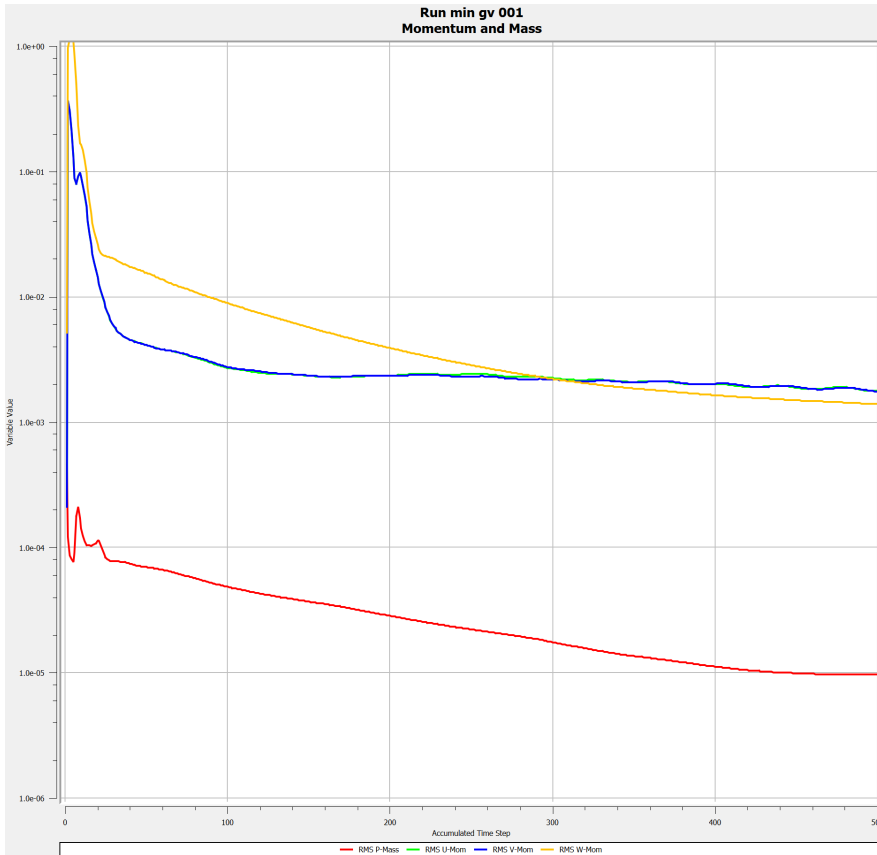The residual plot for the base case is given in Figure G.1.

Figure G.1: Residuals plottet for base case, with 500 iterations.